Hydrogen Gas Sensor Based on a Polymer Optical Microdisk Resonator

by

Mustafa Eryürek

A Thesis Submitted to the
Graduate School of Science and Engineering
in Partial Fulfillment of the Requirements for
the Degree of

Master of Science
in
Optoelectronics and Photonics Engineering

Koç University

August 2013

Koç University

Graduate School of Science and Engineering

This is to certify that I have examined this copy of a master's thesis by

Mustafa Eryürek

and have found that it is complete and satisfactory in all respects,

and that any and all revisions required by the final

examining committee have been made.

Committee Members:

Alper Kiraz, Ph. D. (Advisor)

Ali Serpengüzel, Ph. D.

Erdem Alaca, Ph. D.

Date:

To my parents

ABSTRACT

Hydrogen gas is an attractive energy source since its energy conversion efficiency is higher than conventional oil and its side products after combustion are non–toxic. However, it has a very small lower flammable limit (4% by volume) and its storage is difficult because of small molecular volume. Therefore even low concentration leakages become very dangerous to the public health and the safety of property. Hence, selective detection of small concentrations of hydrogen gas is required. In this work, we propose a hydrogen sensor based on polymer optical microdisk resonators fabricated using UV photolithography. The sensing mechanism relies on the shift of optical whispering gallery modes (WGMs) due to the size change of the resonator in the presence of hydrogen gas. The size change is induced by volume expansion of palladium layer coated on the microdisk resonator. We fabricated microdisk structures together with optical waveguides using SU–8 photoresist on Si substrates possessing a 5 µm–thick thermal oxide. A tunable laser was coupled into the waveguides using end–face coupling. When laser transmission was measured as a function of wavelength, transmission dips were observed revealing the WGMs. A maximum quality factor (Q–factor) of 2000 was measured for the observed WGMs of 200 µm–diameter microdisks. Palladium layer was coated on the fabricated microstructures using lift–off technique. Experiments are now underway for characterizing hydrogen gas sensitivity of these structures. Our estimates reveal sensitivities better than 1000 ppm for the fabricated structures. In parallel to these efforts using microdisks fabricated by UV photolithography, two-photon polymerization was employed for fabricating microdisks and microrings. For these structures, maximum Q–factors of around 120 were measured. Relatively low Q–factors were attributed to small diameters (30 µm) of these structures.

ÖZET

Hidrojen gazının erk verimi kayayağından fazla olduğundan ve yanmasından sonra ortaya çıkan yan ürünlerinin zehirli olmamasından dolayı hidrojen gazı ilgi çekici bir erk kaynağı olmaya başlamıştır. Ancak hidrojen gazının en düşük yanma sınırı hacimce %4'tür ve molekül hacmi küçük olduğundan saklanması zordur. Bu nedenle çok küçük hidrojen sızıntıları bile can ve mal güvenliği açısından çekince oluşturmaktadır. Bu yüzden düşük yoğunluklardaki hidrojen gazının seçici bir şekilde algılanması gerekmektedir. Bu çalışmada morötesi fotolitografisi ile üretilen polimerden yapılmış optik mikrodisk çınlaç tabanlı hidrojen gazı algılayıcısı tasarlanmıştır. Hidrojen gazının ortama verilmesiyle çınlaçların hacminin artması ve optik fısıldayan geçit kiplerinin (FGK) kayması, algılama yönteminin temelini oluşturmaktadır. Çınlaç hacminin artması, çınlaç üzerine paladyum kaplanarak sağlanmaktadır. 5 μm ısıl oksit tabakası olan silisyum alttaş üzerine SU–8 fotorezisti kullanılarak mikrodisk ve dalga kılavuzu yapıları üretilmiştir. Dalgaboyu ayarlanabilir lazerden gelen lazer ışığı optik fiber ile dalga kılavuzunun uçları karşı karşıya getirilerek dalga kılavuzuna aktarılmıştır. Lazerin dalgaboyu değiştirilirken dalga kılavuzundan iletilen lazer ışığının gücü ölçülerek FGK'ların ortaya çıkması sağlanmıştır. 200 μm çapındaki diskler için en yüksek nitelik katsayısı 1400 olarak ölçülmüştür. Mikroyapıların üzerine aşındırma yöntemi kullanarak paladyum kaplaması yapılmıştır. Şimdiki deneylerde bu yapıların hidrojen gazı duyarlılığı ölçülmektedir. Bu yapılar kullanılarak milyonda 1000'den daha az yoğunlukların algılanabileceği öngörülmektedir. Morötesi fotolitografi üretimi denemelerine koşut olarak iki foton ile polimerleştirme yöntemi kullanılarak da mikrodisk ve mikrohalka üretimi yapılmıştır. Bu yapılardan elde edilen en yüksek nitelik katsayısı 120 olarak ölçülmüştür. Bu düşük nitelik katsayısı yapıların çaplarının küçük olmasına bağlanmaktadır (30 μm).

ACKNOWLEDGEMENTS

I would like to express my deepest gratitude to my advisor Professor Alper Kiraz for giving me the opportunity to work with him, his guidance and the experiences I earned throughout my studies. I admire him for being always enthusiastic and for his way of solving problems.

I would like to thank Professors Ali Serpengüzel and Erdem Alaca for joining my thesis committee. I would like to thank Professor Serpengüzel for his help and support regarding the theory of whispering gallery modes and Erdem Alaca for his experience and guidance in the microfabrication techniques.

I would like to thank people from Bilkent University, especially Professors Atilla Aydınlı, Coşkun Kocabaş, Ceyhun Bulutay, Özgür Oktel, Oğuz Gülseren and Dr. Sinan Balcı for their experience, guidance and providing good examples of academics in my undergraduate years. Also, I would like to thank Osman Balcı, Ahmet Bekdemir, Oğuzhan Aydın, Süleyman Şahal, Doğukan Deniz, Önder Akçaalan, Emrah İlbey, Mustafa Fırat and Abdullah Muti for their friendship throughout my undergraduate years.

I would like to thank people who helped me in my research. First, I thank my fellow group members. I thank Yasin Karadağ for his experience dealing with optical fibers, Dr. Nevin Taşaltın for her experience regarding hydrogen sensing, Dr. Alexander Jonáš for his experience in optics and Dr. Yavuz Yüce and Mehdi Aas for their experience, support and guidance. Second, I wish to thank Dr. Cihat Taşaltın for sharing his experience regarding gas sensing, Necmettin Kılınç for his guidance regarding palladium–hydrogen interactions, Selçuk Çakmak for his help and support in building electronic infrastructure for my experiments, Zuhal Taşdemir and Yasin Kılınç for sharing their experience and time in the clean room and Dr. Lóránd Kelemen from Biological Research Center,

Szeged, Hungary for his help and support regarding two–photon polymerization experiments. Third, I would like to thank Can Cihan, Ferda Canbaz, Philipp Heck, Işınsu Baylam, Ersan Özelci, Refik Ergün, Abdullah Bilgin, İbrahim Hocaoğlu, Ersen Beyatlı and Kerem Karakuş for their help, support and friendship. Fourth, I would like to thank my roommate and my best friend, İsmail Yorulmaz. We got over most of the problems together, I learned so much from him and I consider myself very lucky to have a friend like him. Therefore I offer him my deepest gratitude for his support, patience, guidance and encouragement since our freshman year.

Also, I would like to thank my family, especially my parents to whom I dedicate this thesis, for encouraging me for pursuing an academic career in physics.

Last but not least, I would like to thank the Scientific and Technical Research Council of Turkey (TÜBİTAK) for funding this project.

TABLE OF CONTENTS

LIST OF FIGURES

NOMENCLATURE

a	Radius of the microdisk resonator
c	Speed of light in vacuum
FTIR	Frustrated total internal reflection
$\hbar$	Reduced Planck constant
k	Photon wavenumber in the material
k_0	Photon vacuum wavenumber
L	Photon angular momentum
l	Radial mode number
m	Azimuthal mode number
n	Refractive index of material
n_{eff}	Effective refractive index of material
R	Radial part of Ψ
r	Radial parameter in cylindrical coordinates
r_{min}	Minimum distance that mode fields are allowed in a disk resonator
r_{max}	Maximum distance that allows coupling to modes of a disk resonator
SEM	Scanning electron microscope
TPP	Two–photon polymerization
V_{eff}	Effective potential experienced by a photon due to a disk resonator
WGM	Whispering gallery mode
x	Hydrogen concentration in palladium hydride

δ	Phase shift experienced by light
δa	Radius expansion
$\delta\lambda$	Resonance wavelength shift
λ	Wavelength of the excitation light in the material
λ_0	Vacuum wavelength of excitation light
λ_{FSR}	Free spectral range in terms of wavelength
λ_m	Resonance wavelength of azimuthal mode number m
ν_{FSR}	Free spectral range in terms of frequency
ν_m	Resonance frequency of azimuthal mode number m
Φ	Azimuthal part of Ψ
φ	Azimuthal parameter in cylindrical coordinates
Ψ	Solution of Helmholtz equation

Chapter 1

INTRODUCTION

Hydrogen energy draws a lot of attention as an alternative energy source, since it has high energy conversion efficiency and its combustion side products are non–toxic [1]. However, at room temperature, the lower flammable limit of hydrogen gas in air is 4% by volume, which makes hydrogen gas very dangerous for public health and safety of property. Therefore, to avoid any explosions caused by hydrogen gas leakage, hydrogen gas sensors that can quickly respond to small hydrogen concentrations at room temperature are required [2]. In this thesis, a hydrogen gas sensor based on polymer optical microdisk resonators is presented. The chapters are organized as follows. In chapter 1, the importance of hydrogen is explained and a review of hydrogen gas sensors is presented. In chapter 2, operation principle of the proposed sensor is explained. Then in chapter 3, the theory of whispering gallery modes is discussed. Fabrication procedure is presented in chapter 4. In chapter 5, the experimental setup and results are presented. Finally in chapter 6, the conclusion and the outlook are given.

1.1 Importance of Hydrogen

Fossil fuels used along the history are rich in carbon hence they yield CO and CO_2 upon their combustion, causing air pollution and global warming [3]. After wood, the first fossil fuel energy source, the effort was always to make the energy sources more hydrogen–rich so that they become cleaner. Therefore coal, petroleum, propane and methane have been used after wood [3]. In this sequence, the molecular complexity decreases, the molecule becomes more hydrogen–rich and ultimately the fuel becomes cleaner. Methane has carbon, therefore its combustion produces CO_2. On the other hand, the side products of combustion of hydrogen are only water and NO_x [1]. This makes hydrogen a very clean energy source that is often identified as the energy source of the future. Apart from being clean, hydrogen gas is energy–efficient (hydrogen 140.4 MJ/kg, gasoline 48.6 MJ/kg), it is abundant and easy to produce [3]. Therefore many potential applications arise for hydrogen gas, such as power generation for industrial and domestic usage and applications in space [4].

Production of hydrogen can be performed using various methods such as production from hydrocarbons, coal, nuclear energy, wind energy and solar power. Hydrogen production technology has been developed in recent years so that the maximum efficiency in production of hydrogen in a fuel cell has reached up to 60% [3]. Storage after production of hydrogen is more problematic, since hydrogen can penetrate through most of the materials because of its small molecular volume. The storage of hydrogen can be performed using chemical hydrides, complex hydrides or as cryocompressed hydrogen. There are two properties that are used to characterize the storage ability of different methods; volumetric capacity (g/L) and gravimetric capacity (%wt). 20-30 g/L of volumetric capacity and 2-4 wt % gravimetric capacity are achieved using hydrides in the current technology. The cryocompressed and liquid hydrogen storage methods have a little bit better results than the hydride methods; 35-40 g/L of volumetric and 4-4.5 wt % gravimetric capacities. The expected targets for volumetric and gravimetric capacities in a near future are 80-100 g/L and 9-10 wt%, respectively [3].

Hydrogen gas has high diffusion coefficient in air; it is colorless, tasteless and has a wide flammability range (4%-75% by volume). Therefore different types of hydrogen gas sensors attempting to quickly detect hydrogen gas in different concentrations and environmental conditions have been presented in the literature [5].

There is a tremendous effort [5] to introduce hydrogen gas sensors that can work under different environmental conditions such as very low [6] or very high [7] temperatures, very low [8] or very high [9] hydrogen gas concentrations, temperature and humidity fluctuations and in the presence of different chemicals [5]. Some types of hydrogen gas sensors may have more advantages than others, depending on the environmental conditions. Thermal, electrical, mechanical and optical hydrogen sensors, their advantages, disadvantages and operation mechanisms are discussed below [5].

1.2 Hydrogen Gas Sensors Based on a Thermal Response

Thermal response relies on either the thermal conductivity change in the environment or the heat produced by the chemical reaction between H_2 and O_2.

1.2.1 Thermal Conductivity Measurements

Sensors based on thermal conductivity are called as katharometers, which are first used to determine the purity of hydrogen gas [10]. High difference between thermal conductivities of air and hydrogen gas is the underlying principle for thermal conductivity measurement (0.026 and 0.174 W/mK respectively) [5]. Thermal conductivity measurement is sensitive to hydrogen concentrations between 1-100% with short response times (shorter than 20s). However, thermal conductivity is not sensitive to hydrogen concentrations smaller than 1%. In addition, temperature fluctuations or presence of gases having high thermal conductivity such as methane and carbon monoxide introduce noise to the detection signal [5].

1.2.2 Measurement of Heat Produced from H_2–O_2 Reaction

There are two methods to measure produced heat from H_2–O_2 reaction. The first method is called pellistor–type, which relies on the measurement of the electrical resistivity change of a metal such as platinum or palladium due to the heat produced from H_2–O_2 reaction. Pellistor–type sensors are reliably stable under a wide range of environmental conditions such as humidity, temperature and pressure. Also, a quick response time of 8s is achieved [5]. On the other hand, pellistor–type sensors are not hydrogen–selective since they are cross–sensitive to other explosive gases like methane or propane. In addition, pellistor–type sensors require oxygen gas in the environment [5]. The shortest response time reported for pellistor–type sensors in the literature is 0.36 s, which is recorded in the presence of 10000 ppm hydrogen gas concentration [11]. This sensor is fabricated by lithographic techniques and is very compact (2.4 mm by 2.4 mm). Hydrogen selectivity of the device is increased by coating the sensor with a layer of platinum. However, the response time of 0.36 s is recorded at 115^{O}C, and it is not possible to use the sensor at room temperature with the same response time, which is a massive disadvantage of this pellistor–type sensor.

The second method to obtain the heat produced from H_2–O_2 reaction relies on the thermoelectric effect, in which two end points of a conductor that initially have the same temperature are placed in two different cells. The temperature of one cell is kept fixed for reference while the temperature of the other cell increases due to the H_2–O_2 reaction. Resultant temperature gradient between two ends of the conductor causes an electrical potential to build up between these two ends. This potential is measured to obtain the hydrogen concentration in the environment. As opposed to pellistor–type sensors, thermoelectric sensors can operate at room temperature [12]. In addition, if platinum is used as catalyst, the hydrogen selectivity of thermoelectric sensors becomes higher than that of pellistor–type sensors, since platinum only catalyzes combustion of hydrogen at room temperature [13]. On the other hand, at room temperature, the thermoelectric effect is a slow process resulting in long response times. Even advanced designs like crystallized SiGe films or bismuth–telluride P-N junctions have relatively long response times (50s and 30s, respectively) [13, 14].

1.3 Hydrogen Gas Sensors Based on an Electrical Response

The electrical response relies on either an electrochemical reaction or the resistivity change in a hydrogen sensitive material, such as platinum or palladium.

1.3.1 Electrochemical Response

The electrochemical response requires two electrodes to operate: A reference electrode and a sensing electrode. On the sensing electrode, disintegration of hydrogen gas into protons and electrons takes place. The disintegration can then be detected by measuring either the current or the potential between two electrodes, depending on the sensor type. Electrochemical sensors are suitable for room temperature operation. Lower detection limit of electrochemical sensors is 100 ppm. However, their cross–sensitivity to CO and CO_2 and short sensor lifetime are the disadvantages of electrochemical sensors [5].

1.3.2 Resistive Response

Resistive response relies on the resistivity change in a hydrogen–sensitive metal in the presence of hydrogen gas. Due to the expansion of palladium, when exposed to hydrogen, the electrical resistivity of palladium decreases. Using this phenomenon, 75 ms response time is achieved for a concentration range of hydrogen from 2% to 10% at room temperature [15]. However, detection sensitivities in the order of a few ppms are not possible and the temperature fluctuations decrease the accuracy of these detectors.

Resistive response can also be achieved using work function change of a hydrogen–sensitive metal (Pt or Pd) in a Schottky diode. The adsorption or chemisorption of hydrogen gas in the sensitive metal disintegrates H_2 into two H^+ ions (protons). The presence of these protons results a change in the electrical resistance of the sensitive metal. The resistance change can be obtained from the change in the I-V characteristics. Using Schottky diode sensors, hydrogen gas concentrations from ppm level to 30% were detected at room temperature with response times in the order of seconds [16].

1.4 Hydrogen Gas Sensors Based on a Mechanical Response

The mechanical response relies on either an acoustic response or resonance frequency shifts in microfabricated cantilevers.

1.4.1 Acoustic Response

Acoustic response relies on either the sensitivity of piezoelectric materials or the shift of sound velocity in the hydrogen–sensitive material. Measurements using piezoelectric materials rely on the resonance of piezoelectric material under a particular deformation.

The frequency of this resonance is very sensitive to accumulated hydrogen mass on the piezoelectric material. Hydrogen gas detection sensitivity of piezoelectric sensors is high. 8 ppm lower detection limit with 1.5s response time was achieved using piezoelectric-sound-resonance-cavity [17]. Although piezoelectric sensors are sensitive and have a quick response, fluctuations in the humidity and temperature of the environment introduces noise to the detection signal, which is a disadvantage of piezoelectric sensors.

Sound velocity measurement for hydrogen gas sensing has been performed using palladium–hydrogen interaction. If palladium wires are exposed to hydrogen gas, the speed of sound in these wires changes. This change can be employed to detect hydrogen gas. A wide range of hydrogen concentrations between 1-100% were detected with a response time of 30 s at 180^0C [18]. However, precise calibration of speed of sound in material must be performed for accurate detection. In addition, noise level increases with the temperature fluctuations in the environment [5].

1.4.2 Microfabricated Cantilevers

Using mechanical resonance shifts of microfabricated cantilevers [19], it is possible to detect hydrogen gas in the environment. The cantilevers are coated with hydrogen–sensitive material such as palladium. When hydrogen gas is present in the environment, palladium–hydrogen interaction causes a shift in the mechanical resonances of cantilevers. Then this shift is measured to determine the hydrogen gas concentration in the environment [20]. Although cantilever–based sensors are selective, sensitive and compact, their response times are very long (90 s) [21].

1.5 Hydrogen Sensors Based on an Optical Response

The optical response for hydrogen gas sensing takes advantage of either the change in the refractive index of palladium coated on an optical fiber or the effect of a minute volume expansion to an interferometer in the presence of hydrogen gas. The change in the refractive index of palladium can be detected by measuring the transmission from the optical fiber, whereas volume expansion is detected by measuring the change in the interference signal of an interferometer.

1.5.1 Interference Signal

The exposure of hydrogen gas to palladium causes a volume expansion in palladium. This expansion changes both the refractive index of the optical fiber and the optical path length of the light propagating in the optical fiber. The first optical hydrogen gas sensor in the literature exploits this expansion by measuring the interference pattern with Mach–Zehnder apparatus [22]. Room temperature detection of 0.6% hydrogen gas concentration has been achieved with this method. In addition to Mach–Zehnder, Fabry–Pérot and Michelson interferometers are also used in which low detection limits are obtained (0.5%) [23, 24]. However, response times are in the order of a minute, which are relatively slow.

1.5.2 Reflection – Transmission Measurements

The refractive index change of a portion of an optical fiber due to the expansion of palladium coating upon exposure to hydrogen not only affects the interference pattern, but also the transmitted power through the optical fiber. Using this technique, hydrogen concentrations ranging from 1% to 17% are detected at temperatures ranging from –196^{0}C to room temperature with a very fast response time (5 s) [6].

1.5.3 Surface Plasmon Resonances (SPR's)

SPR's are electron–photon interactions formed in metal–dielectric interfaces [25]. Choosing palladium as metal, SPR's can be used as hydrogen gas sensors. They are very sensitive to the refractive index of the metal; therefore the change in the refractive index of palladium, when it is exposed to hydrogen gas can be exploited for hydrogen detection. To detect hydrogen gas using SPR's, either a fiber is coated with palladium [26] or a palladium–coated perfect absorber is used [27]. In both cases, the detection signal is obtained from the change in the reflectivity. Theoretically, plasmonic hydrogen sensors can detect concentrations as low as 0.001% [28]. However, the lowest detected concentration of hydrogen by plasmonic sensors has been 0.5% with a response time 10–50 s [27].

1.6 Proposed Optical Sensing Mechanism

Optical hydrogen gas sensors have several advantages over the other types of hydrogen gas sensors, such as smaller size, more flexibility, higher resistance to other chemicals and quicker responses [29]. In addition, optical quantities like intensity, polarization, phase and frequency supply a wider range of information carriers, generating more optical sensing mechanisms. Frequency is a better information carrier, since frequency information lost due to light–matter interactions is the least as compared to other information carriers. Therefore, studying mechanisms with high spectral sensitivity produces sensitive gas detection devices. The sensing mechanism, presented in this thesis, takes advantage of high spectral sensitivity of optical modes propagating in optical microdisk resonators.

Sensing mechanism relies on the resonance frequency shifts of microdisk resonators. Frequency shifts are provided by coating a thin layer of palladium, a hydrogen–sensitive material, on top of microdisk resonators. The adsorption of hydrogen gas in palladium increases the volume of the microdisk resonator, which results in a resonant frequency shift in the optical mode propagating in the microdisk resonator. The resonant frequency shift is measured to obtain the hydrogen concentration in the environment.

Proposed optical microcavity–based hydrogen gas sensor has several advantages. First, selective detection of hydrogen gas at room temperature is possible, since palladium interacts strongly only with hydrogen at room temperature [26]. Secondly, using microdisk resonators allows building very compact detectors. Finally, detection of small concentrations of hydrogen gas is possible, since the resonant frequencies of optical modes are very sensitive to the size of the microdisk resonator. The aim for the lowest detection limit is in the order of several hundreds ppm. A detailed operation principle is provided in Chapter 2.

Chapter 2

OPERATION PRINCIPLE OF THE PROPOSED HYDROGEN GAS SENSOR

The operation principle of the proposed hydrogen gas sensor takes advantage of the high spectral sensitivity of WGMs to the size of the optical resonators. The size change is employed using an active layer, which is palladium for hydrogen sensing. In this chapter, the palladium–hydrogen interactions are discussed and the operation principle of the sensor is explained.

2.1 Palladium–Hydrogen Interactions

Hydrogen gas is known to have strong interactions with various metals. The reaction between a metal and hydrogen can be ionic, covalent or metallic and the end product is called as metal hydride. Metal hydrides are mostly used for hydrogen storage with sodium, magnesium, lithium, aluminum, iron and nickel [3]. When a metal is exposed to hydrogen, a number of reactions occur. Firstly, the hydrogen gas molecule is adsorbed on the metal surface. Secondly, the hydrogen molecule disintegrates into two hydrogen ions. Thirdly, these ions diffuse into the metal. Fourthly, the ions are settled in the appropriate interstitial sites in the metal. Finally, the hydrogen ions take the reverse steps from four to one to be desorbed from the metal. Palladium is used in this sensor as the active metal for hydrogen sensing. Although palladium is not widely used for storage of hydrogen, mostly because it is expensive, the interaction between palladium and hydrogen is one of the strongest, even at room temperature [26]. In addition, the diffusion coefficient of hydrogen in palladium is three orders of magnitude higher than the metals with the same lattice structure [30].

2.2 Hydrogen in Palladium Lattice

Palladium lattice has the face–centered cubic (FCC) structure. When the hydrogen gas is exposed to the palladium lattice, hydrogen atoms settle in some interstitial sites. There are two types of interstitial sites in a lattice; tetrahedral sites and octahedral sites. These names are given after the geometrical structure that is formed by the atoms surrounding these sites. For instance tetrahedral (T) sites are formed by 4 atoms, in which these atoms generate a tetrahedron. On the other hand, octahedral (O) sites are formed by 6 atoms, in which these atoms generate an octahedron. T sites of an FCC lattice form another FCC lattice and there is one T site per metal atom. O sites of an FCC lattice form a simple cubic lattice and there are two O sites per metal atom.

An O site in the palladium lattice can enclose a spherical atom with radius as big as 70 pm, whereas a T site can enclose an atom with radius only 38 pm. Since the radius of a hydrogen atom is 53 pm, the hydrogen atom chooses to settle in the O site, because it is big enough for the hydrogen atom (see Fig. 2.1).

The settlement of hydrogen atoms in these interstitial O sites causes a volume expansion in the palladium lattice. The lattice parameter of palladium lattice is increased by a certain amount, depending on the concentration of hydrogen. The volume expansion can be fed to an optical resonator, which shows different whispering gallery resonances for different sizes. Therefore, the volume expansion phenomenon is a key to determining the concentration of hydrogen gas in the environment.

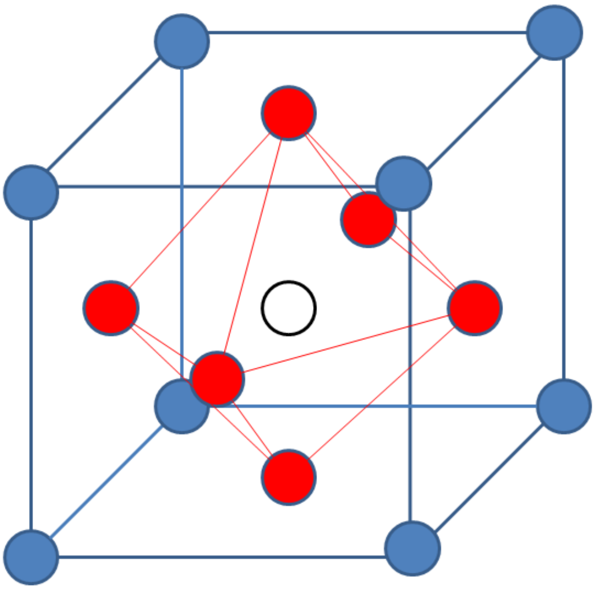

Figure 2.1 Representation of an O site in an FCC lattice. The O site is represented by the black circle in the middle of the octahedron formed by red atoms.

2.3 Phases of Palladium Hydride

Palladium hydride shows two different phases depending on the hydrogen concentration in the environment. We can define a parameter to denote the hydrogen concentration; x = H/Pd. For small concentrations of hydrogen (x < 1.5%) the palladium hydride is defined to be in its α–phase. In α–phase, the lattice parameter of palladium is increased from 3.890 Å to 3.895 Å. Since the hydrogen concentration is small, the volume expansion in the palladium lattice is reversible, i.e., if the hydrogen is removed from the environment, then the palladium lattice shrinks to its original state. This reversible deformation is called elastic deformation. On the other hand, if the hydrogen concentration is high (x > 60%) the palladium hydride transforms into β–phase. In this phase the lattice parameter becomes 4.025 Å. The deformation caused by the volume expansion of palladium in β–phase is irreversible, i.e., once the lattice expands, it stays expanded even if the hydrogen is removed from the environment. This irreversible deformation is called plastic deformation. For medium concentrations (1.5% < x < 60%) α–phase and β–phase coexist [31]. However, this concentration region is valid for room temperature. As the temperature is increased the mixed–state concentration region becomes smaller and smaller. After a critical temperature (around 300^{0}C) there is no mixed state in palladium hydride, it is either α–phase or β–phase (see Fig. 2.2).

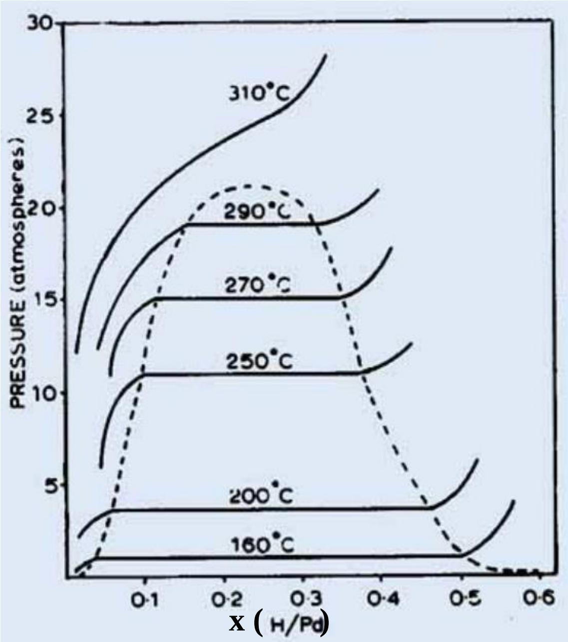

Figure 2.2 Phase diagram of palladium hydride for different temperatures. The mixed-phase state only exists under the dashed curve. The left side of the diagram corresponds to the α–phase and the right side to the β–phase [32].

2.4 Hysteresis

Existence of mixed–phase state causes different response curves for increasing and decreasing hydrogen concentrations (see Fig. 2.3). This phenomenon is called as hysteresis which is an undesirable property for a sensor. In the former topic the effect of increasing temperature on the phase transition is discussed. Therefore the temperature can be increased over the critical temperature to avoid hysteresis. Also, using certain alloys of palladium can also prolong the transition from α–phase to β–phase [33].

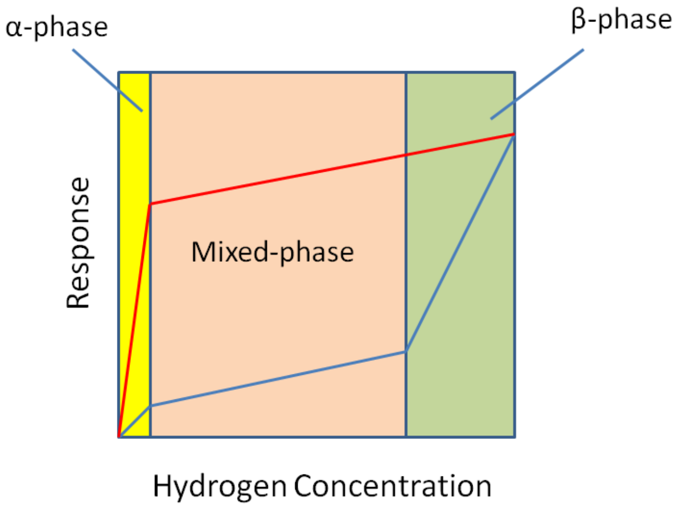

Figure 2.3 The sketch of the phase diagram of palladium hydride. The lower curve represents increasing hydrogen concentration and the upper curve represents decreasing concentration. The hysteresis loop is observed because of the presence of mixed–phase state.

2.5 Operation Principle of the Proposed Hydrogen Sensor

Operation of the hydrogen sensor is based on the spectral shift of WGMs due to the size change of the microdisk resonator, which is induced by the expansion of the palladium layer upon hydrogen exposure (see Fig. 2.4). First, the transmission spectrum of the device is measured with 0% hydrogen concentration for reference. Then the hydrogen concentration will be increased gradually and the transmission spectrum will be measured for every step. Maximum hydrogen concentration, which can be introduced to the system, is 1% and it can be decreased down to 100 ppm by mixing 1% hydrogen gas with nitrogen gas. Therefore, the phase of palladium hydride remains purely in the α–phase, and there is no phase transition. Absence of phase transition removes the hysteresis. Also, the sensor can be used numerous times, since in α–phase palladium deforms elastically.

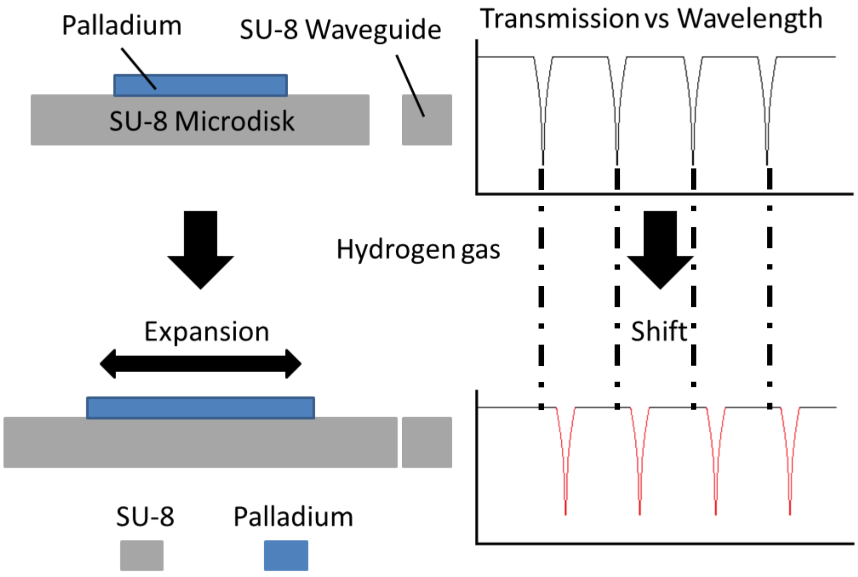

Figure 2.4 Sensing mechanism of the sensor device.

2.6 Estimation of the Lowest Detection Limit

The lowest detection limit of the sensor depends on the smallest detectable resonance shift. This shift can be estimated starting from

$$\frac{\delta\lambda}{\lambda} = \frac{\delta a}{a} \tag{2.1}$$

where λ is the wavelength, $\delta\lambda$ is the wavelength shift, a is the radius of the resonator and δa is the relative increase in the radius of the resonator. Resonators fabricated using UV photolithography have a =100 µm, and the laser light for measurement has λ =1550 nm. Assuming our spectral resolution $\delta\lambda$ is 0.1 nm, then δa becomes 6.5 nm. Using a palladium coating with radius 85 µm and assuming 0.13% radius expansion upon exposure to 1.5% hydrogen concentration [31], the radius expansion becomes 110.5 nm. Therefore, it is possible to detect hydrogen concentrations as low as 900 ppm. This value can be further improved using higher spectral resolution ($\delta\lambda$ < 0.1 nm).

Chapter 3

OPTICAL WHISPERING GALLERY MODES

The optical microcavity hydrogen gas sensor presented in this thesis relies heavily on the optical WGMs of microcavities. The explanation of WGMs was in 1910, when Lord Rayleigh described the sound waves travelling at the inner concave surface of St. Paul's Cathedral [34]. The optical analogue of these WGMs requires an optical microcavity and a laser light. As in the case of sound waves travelling in St Paul's Cathedral, laser light propagates at the inner edge of an optical microcavity (see Fig. 3.1). There is a certain set of frequencies allowed for propagation inside the microcavity, which are called as resonance frequencies. High sensitivity of these resonance frequencies on the size of the microcavity can be exploited for sensing applications. Coating the microcavities with a thin layer of palladium is the key to obtaining hydrogen–selective operation of the device at room temperature. The interaction between hydrogen and palladium causes a volume expansion in the microcavity, which induces a shift in the resonance frequencies. Therefore, it is possible to determine the hydrogen concentration in the environment by measuring the resonance frequency shift.

A microdisk resonator can be considered as a 1D waveguide folded onto itself. The 1D waveguides are suitable for transportation of light, whereas the 2D microdisk resonators are suitable for trapping light for a certain amount of time. This trapping results very high optical power confined in a very small geometry leading to very interesting applications.

Unlike waveguides, the microdisk structure has periodic boundary conditions i.e. the phase of the propagating light must be preserved during the whole trip of light for all points of the resonator. This requirement results in the following equation, which is also known as the resonance condition:

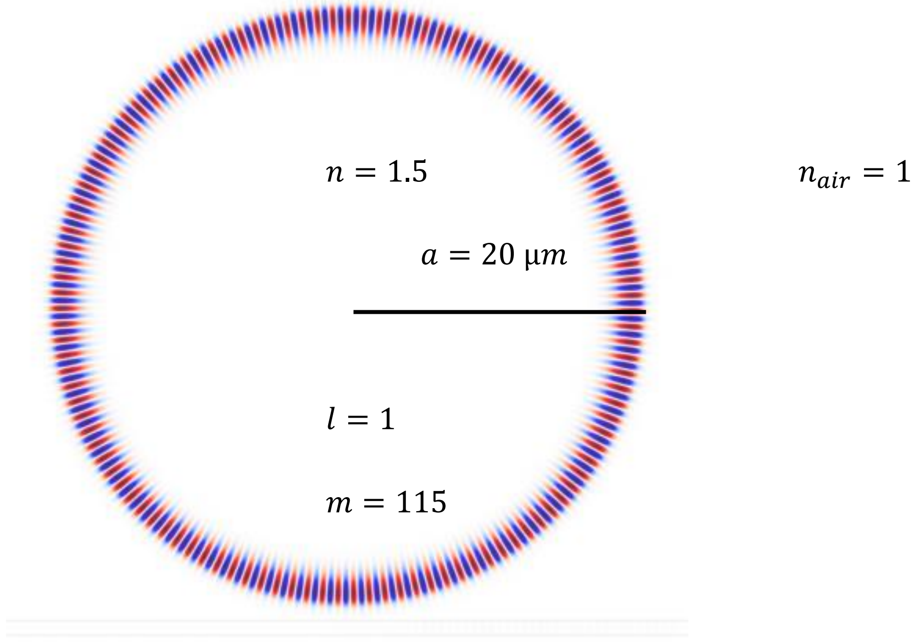

Figure 3.1 A simulation of a WGM propagating inside a disk resonator. Radial mode number, $\boldsymbol{l}$ is 1 and azimuthal mode number m is 115.

$$2\pi a = m\lambda_m \tag{3.1}$$

where a is the radius of the resonator, m is the azimuthal mode number and λ_m is the corresponding resonant wavelength of the mth azimuthal mode. Wavelength in the cavity,

λ_m, is related to the vacuum wavelength λ_0 via $\lambda_m = \frac{\lambda_0}{n_{eff}}$ where n_{eff} is the effective refractive index. The effective index depends on the refractive indices of the resonator and the surrounding medium. In addition, the mode number changes the effective index slightly, since different mode numbers have different mode profiles, this results in different ratios of light intensity in the resonator to light intensity in air.

3.1 The Quality Factor

The quality factor (Q–factor) of a resonator is defined as the number of optical periods experienced by light in the corresponding resonator without being absorbed, scattered or radiatively leaked out of the cavity. The absorption rate can be controlled by the choice of material. Using materials that are transparent for the wavelength of the light reduces the absorption loss and increases the overall Q–factor. Scattering occurs because of the impurities in the resonator or surface roughness of the surface of the resonator. Applying more sophisticated fabrication techniques decreases the scattering loss. On the other hand, radiative loss is a fundamental loss, which occurs because the light inside the cavity is coupled out to the radiation modes of the cavity. The total Q–factor (Q_{TOT}) of the resonator is given by

$$\frac{1}{Q_{TOT}} = \frac{1}{Q_{abs}} + \frac{1}{Q_{scat}} + \frac{1}{Q_{rad}} \tag{3.2}$$

where Q_{abs}, Q_{scat} and Q_{rad} represent the absorption, scattering and diffraction Q–factors, respectively. The value of Q_{TOT} is dominated by the smallest Q–factor among Q_{abs}, Q_{scat} and Q_{rad}.

3.2 The Free Spectral Range

The resonance frequencies of optical microdisk resonators are separated by a certain amount, which is called as the free spectral range (FSR). Calculation of FSR for a Fabry–Pérot cavity is given in [35]. A similar result can be obtained for a disk cavity.

Let δ be the phase acquired for one optical round–trip for a light with a vacuum wave–vector k_0. The relation between δ and k is given by

$$\delta = k_0 2\pi a n \tag{3.3}$$

where a is the radius of the disk and n is the refractive index of the disk medium. Resonance occurs if $\delta = 2\pi m$, which reveals the same results as the resonance condition $2\pi a = m\lambda_m$. Substituting $k_0 = \frac{2\pi\nu_m}{c}$ and cancelling out the common terms we have

$$\frac{2\pi\nu_m}{c} a n = m \tag{3.4}$$

where ν_m is the m$^{\text{th}}$ optical resonance frequency of the disk resonator. The resonance frequencies are separated uniformly, i.e. $\nu_m = m\Delta\nu$. Therefore we get

$$\Delta\nu = \frac{c}{2\pi a n} = \nu_{FSR} \tag{3.5}$$

We can obtain the free spectral range in terms of the wavelength (λ_{FSR}) by starting from $\nu_0 = \frac{c}{\lambda_0}$. If we take a derivative with respect to ν, we obtain $\Delta\nu = -\frac{c}{\lambda_0^2}\Delta\lambda$. We disregard the minus sign, since we are interested in the absolute value of the separation between adjacent resonance wavelengths. Hence $\Delta\lambda$ becomes

$$\Delta\lambda = \frac{\lambda_0^2}{2\pi a n} = \lambda_{FSR} \tag{3.6}$$

3.3 Quantum Mechanical Analogue

Helmholtz Equation for 2D polar coordinates is given by

$$\frac{1}{r}\frac{\partial}{\partial r}\left(r\frac{\partial \Psi}{\partial r}\right)+\frac{1}{r^2}\frac{\partial^2 \Psi}{\partial \varphi^2}+k^2\Psi=0 \tag{3.7}$$

After applying separation of variables method by introducing $\Psi(r,\varphi)=R(r)\Phi(\varphi)$we have

$$\frac{1}{r}\frac{\partial}{\partial r}\left(r\frac{\partial R}{\partial r}\right)\Phi+\frac{1}{r^2}R\frac{\partial^2 \Phi}{\partial \varphi^2}+k^2R\Phi=0 \tag{3.8}$$

By imposing $\Phi=\mathrm{e}^{\pm \mathrm{im}\Phi}$, we can write $\frac{\partial^2\Phi}{\partial\varphi^2}= -\pm m^2\Phi$. Then,

$$\frac{1}{r}\frac{\partial}{\partial r}\left(r\frac{\partial R}{\partial r}\right)\Phi-\mathrm{m}^2\frac{R\Phi}{r^2}+k^2R\Phi=0 \tag{3.9}$$

By dividing with $R\Phi$ we have

$$\frac{1}{Rr}\frac{\partial}{\partial r}\left(r\frac{\partial R}{\partial r}\right)-\frac{\mathrm{m}^2}{r^2}+k^2=0 \tag{3.10}$$

Now, we are ready to make an analogy to Schrödinger’s equation by adding and subtracting k_0^2:

$$\frac{1}{Rr}\frac{\partial}{\partial r}\left(r\frac{\partial R}{\partial r}\right)-\frac{\mathrm{m}^2}{r^2}+k^2-k_0^2+k_0^2=0 \tag{3.11}$$

By using $k_0^2=n^2k^2$Helmholtz equation becomes

$$\frac{1}{Rr}\frac{\partial}{\partial r}\left(r\frac{\partial R}{\partial r}\right)+k_0^2-\left[k_0^2(1-n^2)+\frac{m^2}{r^2}\right]=0 \tag{3.12}$$

The term in brackets corresponds to the potential term in Schrödinger equation. Therefore it is called the effective potential;

$$V_{eff}(r) = \left[k_0^2(1 - n^2) + \frac{m^2}{r^2}\right] \tag{3.13}$$

Plot of the effective potential is given in Fig. 3.2.

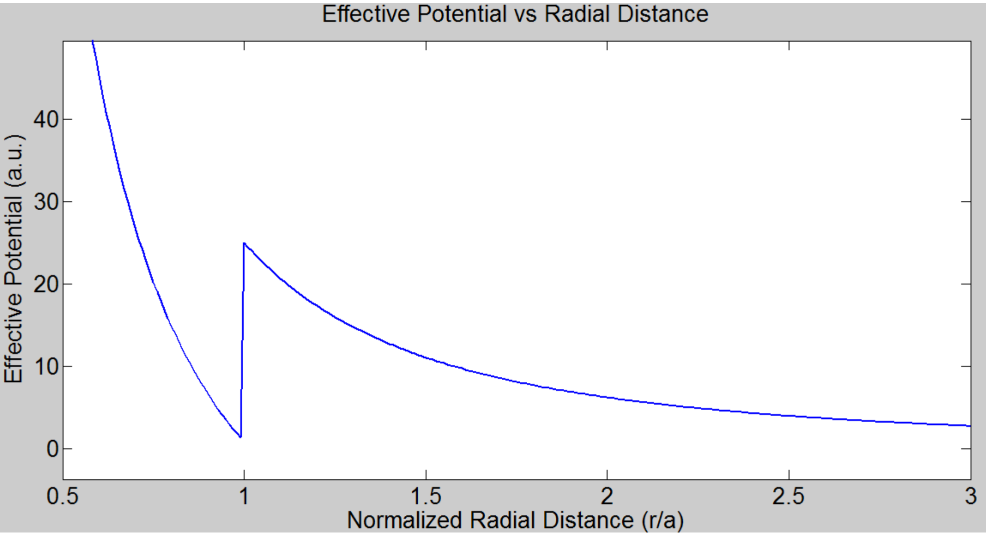

Figure 3.2 Corresponding potential of quantum mechanical analogue of a microdisk resonator. Parameters are $\boldsymbol{\lambda_0 = 1.55}$ µm, $\boldsymbol{n = 1.572}$, $\boldsymbol{m = 50}$ and $\boldsymbol{a = 10}$ µm

From Fig. 3.2, we deduce that the lowest radial order mode corresponds to the inner edge of the microdisk. On the other hand, higher radial order modes can have longer evanescent tails, since the potential well is shorter. Therefore, higher radial order modes tend to couple radiation modes more easily. As a result, the Q–factors of higher radial order modes are lower than the Q–factor of the fundamental mode. In addition, the higher radial order mode can elongate towards the center of the disk. However, there is a limit,

r_{min} for this elongation, which can be found using the angular momentum quantization condition, i.e.,

$$L = \hbar m = \hbar a k_0 \Rightarrow m = a k_0 \tag{3.14}$$

It should be noted that the m in the effective potential is the same m as in the angular momentum quantization. Using $V_{eff}(r = r_{min}) = V_{eff}(r = a)$ we have

$$\frac{m^2}{a^2} = \frac{m^2}{r_{min}^2} + k_0^2 - k^2 \tag{3.15}$$

Now substituting $m = a k_0$ we obtain

$$\frac{a^2 k_0^2}{a^2} = \frac{a^2 k_0^2}{r_{min}^2} + k_0^2 - k^2 \tag{3.16}$$

The wave–vector outside of the disk (k) can be removed from the equation since the wave–vector inside (k_0) and outside (k) are related via $k = k_0 n$. Therefore we obtain

$$\frac{a^2 k_0^2}{a^2} = \frac{a^2 k_0^2}{r_{min}^2} + (1 - n^2) k_0^2 \tag{3.17}$$

After the cancellations the equation becomes

$$1 = \frac{a^2}{r_{min}^2} + 1 - n^2 \tag{3.18}$$

From which we find the minimum distance that a mode field can penetrate

$$r_{min} = \frac{a}{n} \tag{3.19}$$

Mode profiles are restricted to $\left(\frac{a}{n} \leq r \leq a\right)$. The region where no mode is allowed $\left(0 \leq r \leq \frac{a}{n}\right)$ is called the caustic region.

There is another important point on the effective potential, which defines the maximum distance that allows excitation of WGMs inside the resonator, r_{max}. A similar calculation can be performed for r_{max}, which results $r_{max} = an$. Therefore the coupling region is restricted to $(a \leq r \leq an)$.

3.4 WGM Simulations

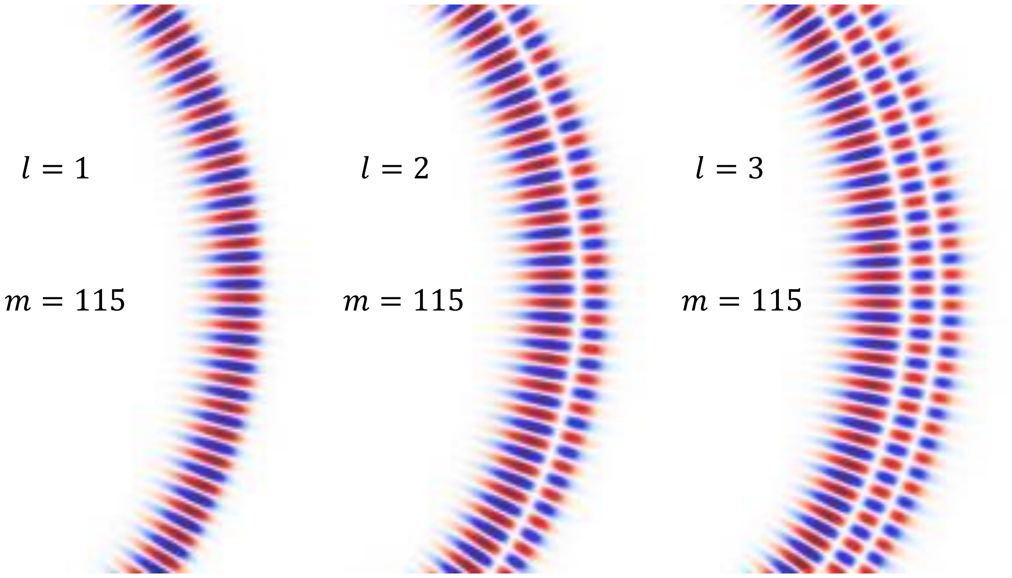

Figure 3.3 MEEP simulation of the first three radial modes for a 20 µm–radius disk. Azimuthal mode number m is 115 for all three cases. As the radial mode number increases, the mode profiles tend to elongate towards to center. In addition, modes elongate to the outside of the disk which causes more coupling to radiation modes.

The resonance wavelength changes for different radial mode numbers. MEEP (MIT Electromagnetic Equation Propagation) simulation is performed for different radial modes and three modes found in a wavelength span of 20 nm for a 20 μm–radius disk resonator [36] (see Fig. 3.3)

For different azimuthal number, (m), there are different resonance wavelengths that satisfy the resonance wavelength condition, as in the case of radial modes. A Matlab simulation is performed to find the resonance wavelengths. However, both resonance wavelength and the radius of the disk are swept in this case [37] (see Fig. 3.4).

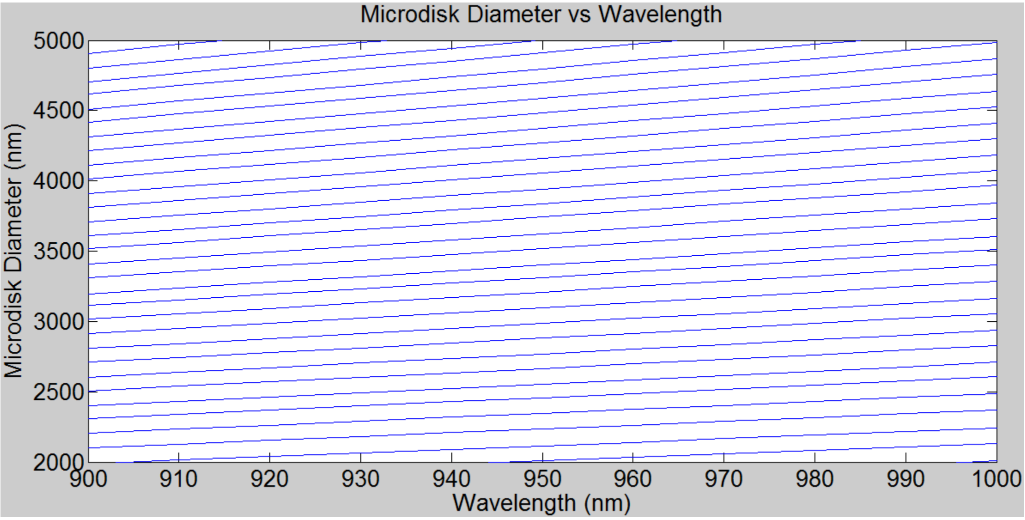

Figure 3.4 Resonance wavelengths for different diameters of the microdisk resonators.

3.5 Coupling Schemes to WGMs of Microcavities

The laser light to be coupled to the WGMs of microcavities is initially in an optical fiber. Excitation of a WGM requires an overlap between the mode profile of the WGM and the evanescent field of the light propagating in the fiber. A standard bare fiber has an outer diameter of 125 μm. Since the evanescent field can only reach a maximum distance of several wavelengths, it is impossible to excite WGMs using a bare fiber. There are three methods by which successful excitation of WGMs can be performed: Excitation using a prism, a tapered fiber, or a waveguide.

3.5.1 Excitation of WGMs Using a Prism

The WGMs of a microcavity can be excited using a prism-coupled configuration (see Fig. 3.5). This can be achieved using a phenomenon called frustrated total internal reflection (FTIR), which is analogous to the tunneling effect in quantum mechanics. The laser light is send to a prism with an incidence angle greater than the critical angle so that the total internal reflection can occur in the prism. However, if a resonator is placed very close to the prism, the light can couple to the resonator because of FTIR and the coupling efficiency depends on the separation. An optical energy transfer over 75% is achieved using prism–coupled excitation [38].

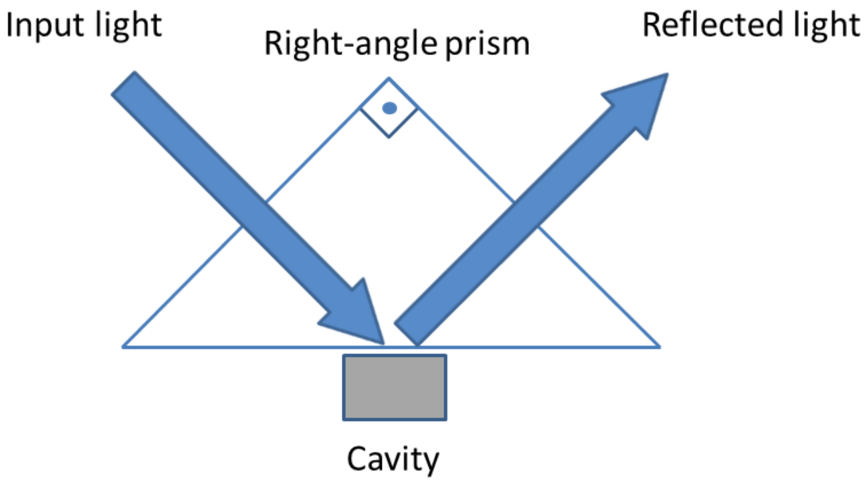

Figure 3.5 A prism–coupled excitation scheme which excites the WGMs of a square cavity.

3.5.2 Excitation of WGMs Using a Tapered Fiber

When an optical fiber is tapered, it is possible to excite WGMs (see Fig. 3.6). The width of the fiber must be small enough to ensure overlap between the evanescent field of the light and the mode profile of the WGM. However, scattering loss may be very high unless the width of the tapered region is varying slowly. Such tapers are called as adiabatic tapers and they are required for obtaining good mode–matching between the wide and narrow parts of the fiber. Since good adiabatic tapers are difficult to produce, careful adjustment of tapering parameters must be performed for low optical loss in the tapered fiber region.

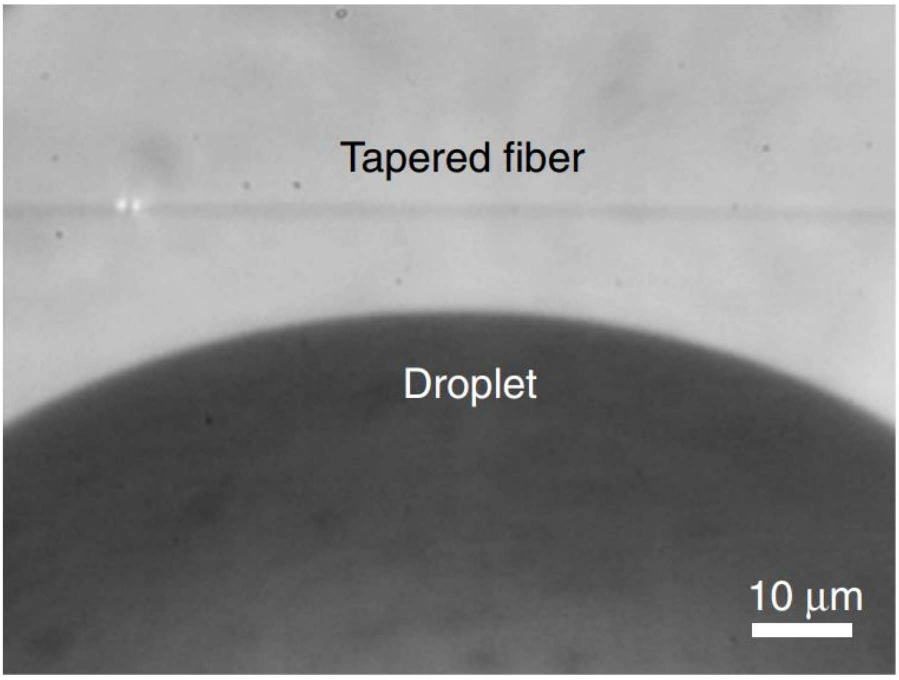

Figure 3.6 Light coupling from a tapered fiber to a spherical droplet resonator [39].

3.5.3 Excitation of WGMs Using a Waveguide

It is possible to excite WGMs by coupling the laser light from the fiber to a waveguide, and then coupling the light from the waveguide to the WGMs of the resonator. Microfabrication techniques have enough spatial resolution to ensure satisfactory coupling between the waveguide and the WGM in which the coupling theory is given in [40]. The difficulty of this method is coupling the light between the optical fiber and optical waveguide. Two different methods are presented in the literature to achieve coupling between the fiber and the waveguide:

3.5.3.1 End–Face Coupling

Fine positioning stages are used for the end–face coupling so that the fiber can be aligned exactly opposite to the waveguide. The end–face coupling method is easy, but the coupling efficiency is low because the core diameter of the fiber is larger than the width of the waveguide. This dimensional mismatch can be eliminated by using a lens between the fiber and the waveguide; however, due to the different mode profiles of the fiber and the waveguide, the insertion loss is high. The end–face coupling method is suitable for applications that do not require high coupling efficiency. In this work, end–face coupling is employed for light coupling between optical fibers and optical waveguides.

3.5.3.2 Coupling with a Grating

Vertical coupling from the optical fiber to the waveguide can be achieved by inserting a grating structure between the fiber and the waveguide. A fiber is placed almost vertically on top of the grating. If the fiber is exactly perpendicular to the waveguide, secondary reflections will couple into the fiber causing noise in the detection signal. Using different diffraction orders the fiber can be placed several degrees (usually about 10 degrees) off from the surface normal. The grating supplies the required horizontal component of the momentum of the light so that the light can propagate in the horizontal direction in the waveguide. The alignment between the grating and the fiber is important to achieve a high coupling efficiency. 70% coupling efficiency is achieved using a grating coupler [41]. This value is further increased to 92% with the help of distributed Bragg reflector (DBR) [42]. The schematic configurations of end–face coupling and grating coupler are given in Fig. 3.7.

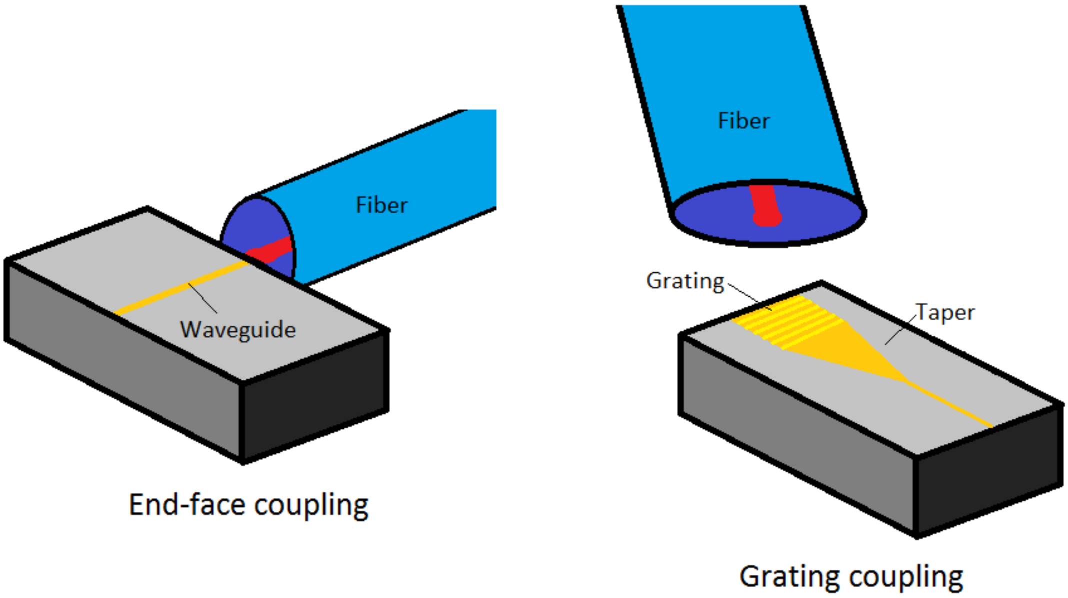

Figure 3.7 End–face coupling and grating coupler comparison. Since the waveguide is much smaller than the grating region, the alignment tolerance of end–face coupling is much less than the grating coupler. However, the taper region after the grating must be adiabatic and designed carefully to get minimum loss from the grating to the waveguide.

Grating structures must be fabricated wide enough to avoid the dimensional mismatch between the fiber core and the waveguide width. However, the width of the waveguide is much smaller and the width of the structure must be adiabatically decreased to obtain minimum loss between wide and narrow waveguide regions (see Fig. 3.7). The transmission can also be collected by using another grating, called the out-coupler grating, onto which a collection fiber is placed.

Once the laser light is coupled into the waveguide, coupling to a WGM can be performed in two ways, depending on the relative position of the waveguide with respect to the mirocavity (see Fig. 3.8). If the waveguide is at the same horizontal level as the microcavity, the coupling is called horizontal coupling. On the other hand, if the waveguide is not at the same horizontal level, but just above or below the edge of the microcavity, the coupling is called vertical coupling. The vertical coupling configuration requires more fabrication steps than that of the horizontal coupling configuration. However, the vertical coupling scheme provides precise control over the optimum distance between the waveguide and the microcavity.

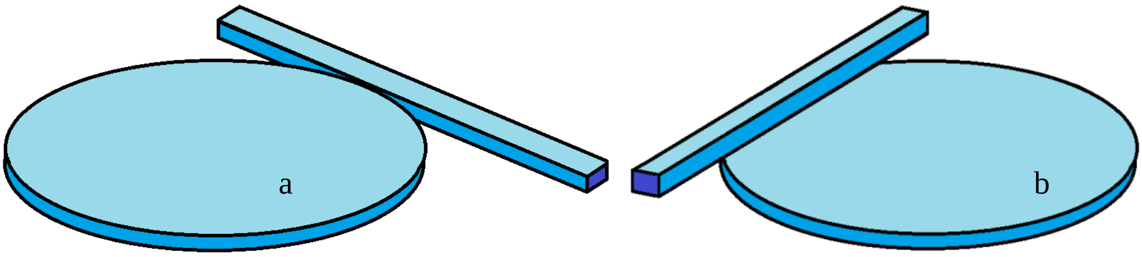

Figure 3.8 a) Horizontal and b) vertical coupling schemes.

Chapter 4

MICROFABRICATION OF OPTICAL MICRODISKS AND WAVEGUIDES

4.1 Introduction

The fabrication of optical elements is performed using UV photolithography which provides 2 μm resolution in the lateral direction. This resolution is enough for obtaining sufficiently narrow disk–waveguide gaps and sufficiently narrow waveguides. However, the surface smoothness of the microresonator edges is not good enough to obtain high optical quality factors. Therefore two–photon polymerization method is employed to increase the smoothness.

In both methods, SU–8 is chosen as the material for fabrication of the microdisk and waveguide structures (see Fig. 4.1). SU–8 is a negative–tone photoresist that has the highest sensitivity at 365 nm excitation wavelength [43]. The choice of SU–8 as the photoresist of the microfabrication procedure has three main reasons. Firstly, development time of SU–8 is not a critical parameter since SU–8 is a negative–tone photoresist. Parts of SU–8 exposed to UV light undergo cross–linking, which causes exposed parts to be insoluble in the developer. Therefore, there is no upper limit for the development time. Secondly, SU–8 is a very adhesive photoresist which ensures fabrication of mechanically stable devices. A good stability of SU–8 can be achieved by a simple low temperature baking process [44]. Another important mechanical property of SU–8 is its elasticity, which is required for obtaining reusable devices. Volume increases and decreases during hydrogen gas sensing may introduce cracks in the optical microdisks. However, high elasticity of SU–8 prevents formation of cracks ensuring fabrication of reusable devices. Finally, SU–8 is a convenient material to fabricate optical waveguides and microdisks, because it has excellent optical properties. Fundamental condition for waveguiding requires that the refractive indices of the waveguide and microresonator must be higher than the refractive index of the substrate. The refractive index of SU–8 is 1.573, whereas the refractive index of SiO_2 is 1.443 at λ=1550 nm [45]. Therefore, SU–8 structures on top of a SiO_2 substrate are suitable for waveguiding. In addition, low optical loss at the operation wavelength is required. The loss of SU–8 at λ=1550 nm is 4 dB/cm [46], which makes SU–8 suitable for sensing purposes.

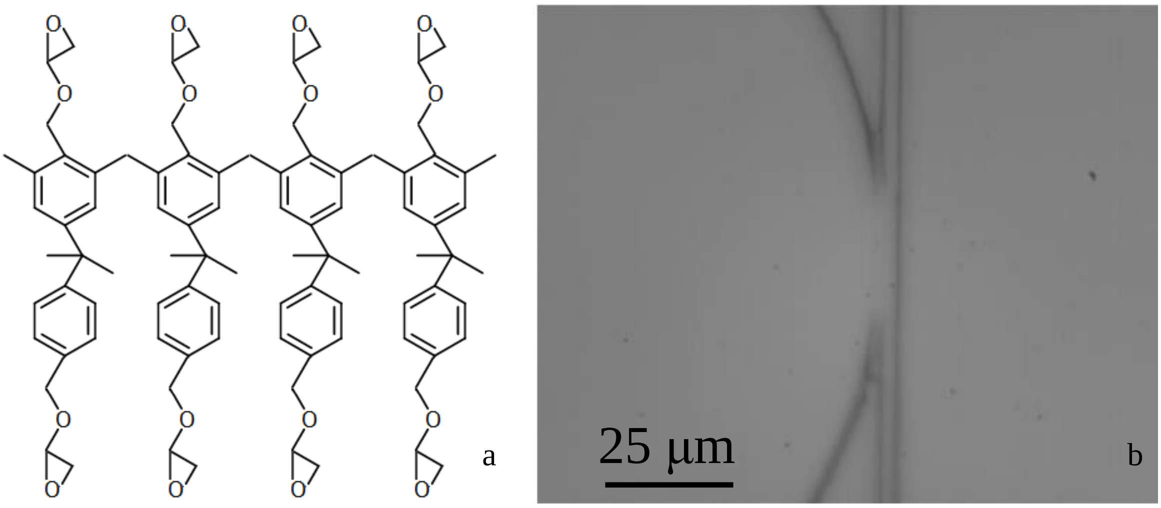

Figure 4.1 a) The monomer of SU–8. b) Fabricated microdisk and waveguide structure.

4.2 Fabrication Flow of Microdisk and Waveguide Structures Using UV Lithography

Standard UV photolithography technique is used for the microfabrication of microdisks and waveguides [19]. After the wafer surface is cleaned with piranha solution (1:5 H_2SO_4–H_2O_2), spin–coating of SU–8 is performed at 3000 rpm for 60s. Spin coating parameters are chosen to obtain around 2 μm–thickness for SU–8. An ideal spin–coating is expected to give a uniform thickness over the whole wafer surface as specified by the manufacturer (see Fig. 4.2). However in practice, the thickness of the SU–8 layer obtained after spin coating is not uniform over the whole wafer surface and it varies in the range between 1.5 to 2.5 μm. The sketch of the fabrication flow is given in Fig. 4.3.

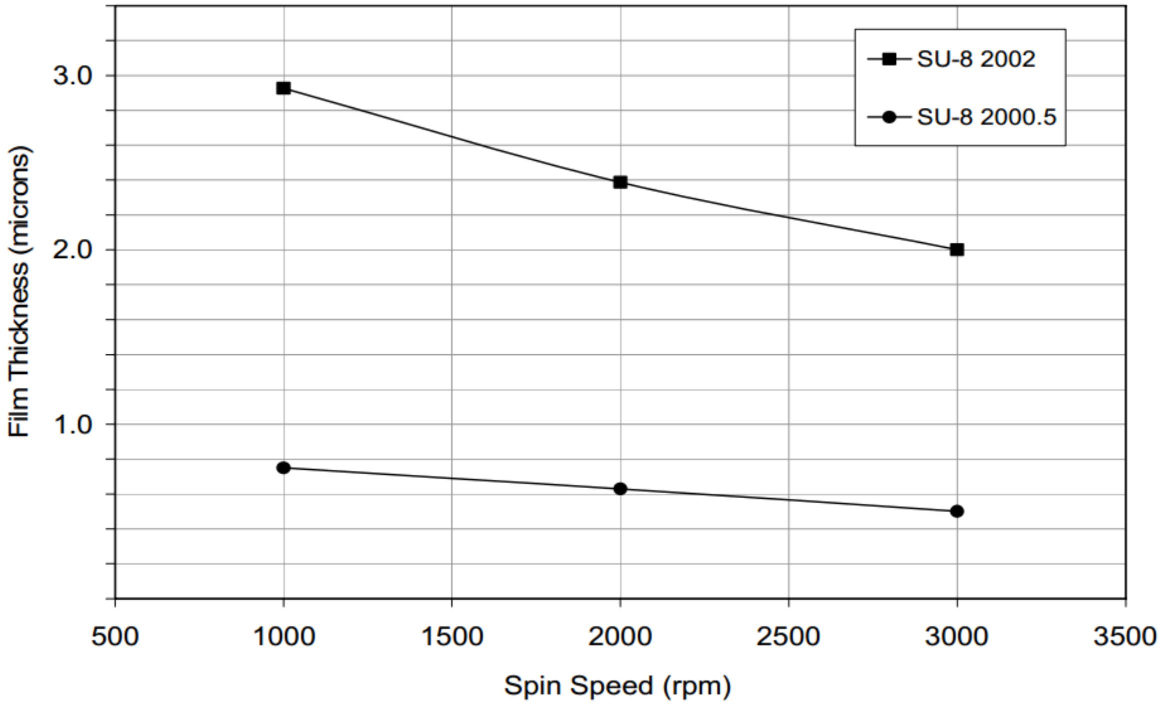

Figure 4.2 Variation of film thickness of SU–8 2000.5 and 2002 with respect to spin coating speed [47].

After spin coating the wafer is soft–baked at 95^{O}C for 60 s. Soft–bake step is required for two reasons, the removal of solvents in SU–8 is required and good adhesion must be satisfied between SU–8 and wafer surface. After soft–bake step, UV exposure is performed with a photomask, which creates a virtual image of the photomask on the SU–8 layer. The optimum exposure time changes depending on the temperature and humidity of the clean room environment. Therefore, a range of exposure times from 15 s to 35 s is applied. After UV exposure, post–exposure bake (PEB) is applied at 95^{O}C for 60 s to ensure the cross–linking of the exposed parts of SU–8 and provide a good adhesion of SU–8 to the wafer surface [43].

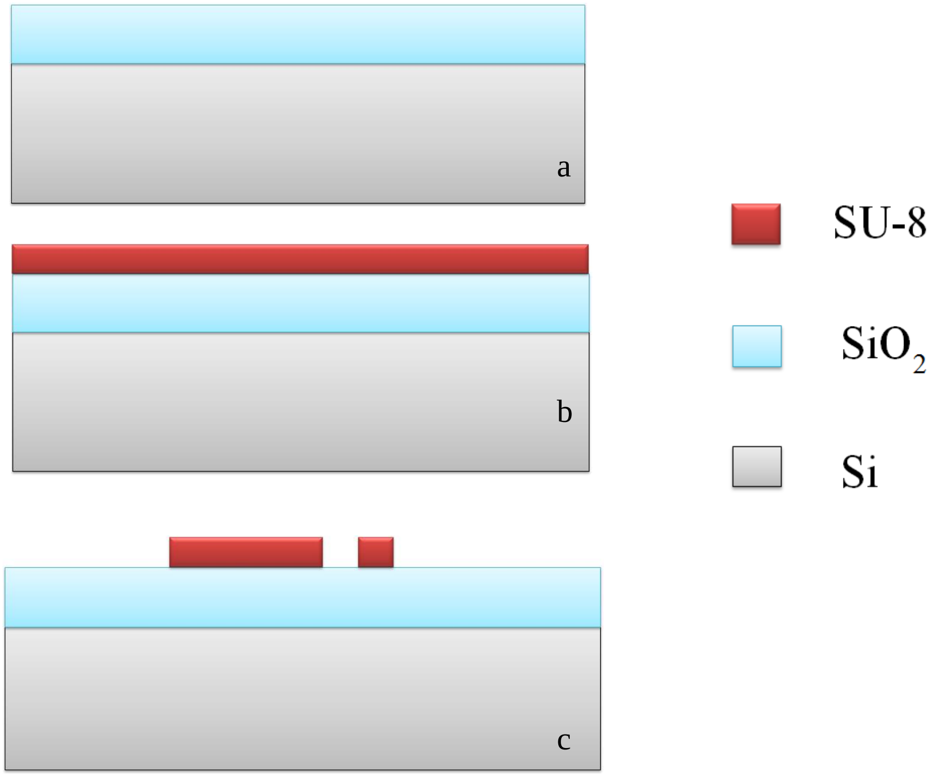

Figure 4.3 Fabrication steps of microdisk and waveguide structures. a) Removal of organic residue from the wafer surface. b) Spin coating of SU–8. c) Formation of SU–8 microdisk and waveguides after exposure and development.

The virtual image created in the exposure and PEB steps is converted into a real image in the development step. SU–8 developer is a specific chemical that can remove the unexposed regions of SU–8 without damaging the exposed regions. Once exposed, SU–8 is insoluble to the developer since the exposed regions of SU–8 are cross–linked. Therefore, there is no upper time limit for the development step. 60 s of development time is applied in the fabrication. Developer residue left on the wafer surface is removed by isopropyl alcohol (IPA). Then wafer is washed with deionized (DI) water to remove IPA. DI water is removed by blowing nitrogen and fabricated structures are irreversibly stabilized on the wafer surface applying hard bake step at 150^{0}C for 5 minutes.

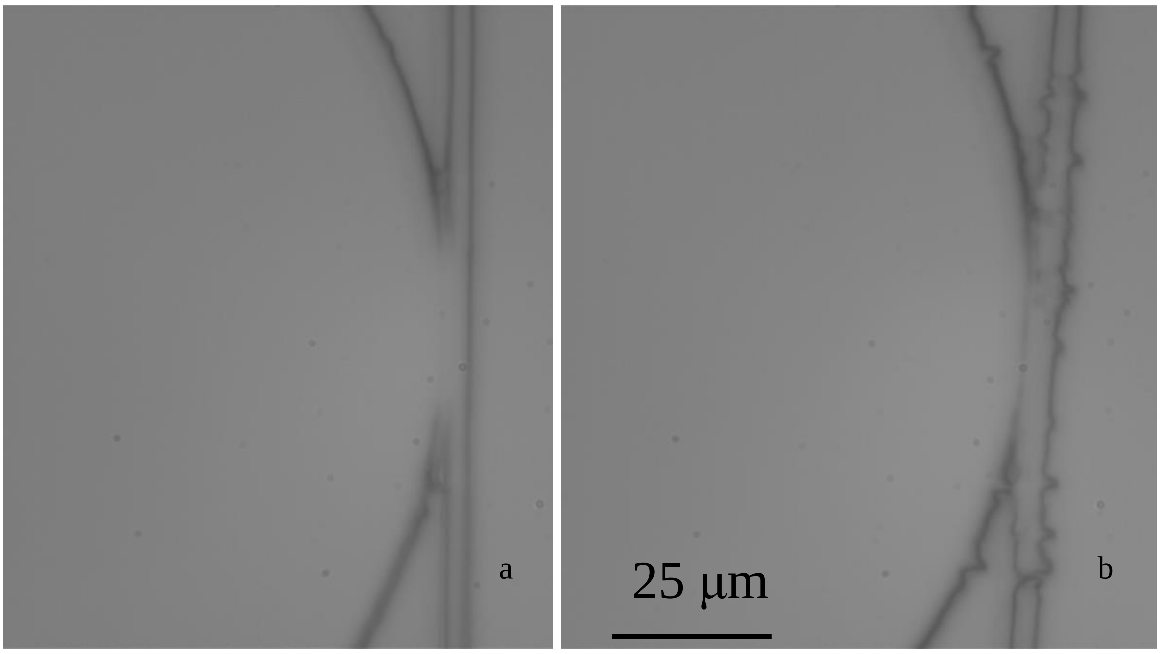

Figure 4.4 Comparison of two samples fabricated with the same fabrication parameters, but in different days. The change in the quality is attributed to the changes in the environmental conditions.

Although the same fabrication parameters are used for fabricating the samples, the changes in the environmental conditions from day to day result different fabrication quality. A good sample should have smooth disk edge, straight waveguide and a good gap region to obtain good transmission measurement (see Fig. 4.4-a). On the other hand, if the disk and waveguide have some imperfections that deviate from the image of the photomask, it becomes difficult to get a measurement from the sample (see Fig. 4.4-b).

4.3 Fabrication Flow of Palladium Coating Using Lift-off Technique

After the fabrication of microdisks, palladium is coated on the microdisks as the hydrogen–sensitive layer. Lift–off process is used for palladium coating [19]. Firstly, AZ 9260 photoresist is spin–coated on prefabricated SU–8 microdisks as a sacrificial layer. Secondly, a UV exposure is applied using a photomask, which is aligned to the pre-fabricated SU–8 microdisks, so that palladium microdisks and SU–8 microdisks will be concentric. Since palladium is a metal, it has a high imaginary refractive index, causing high optical loss. Therefore palladium layer must not overlap with WGMs propagating in SU–8 microdisks. This is achieved by fabricating palladium microdisks smaller than SU–8 microdisks. Precise alignment ensures having concentric microdisks, which is required for high quality factor. Thirdly, the sacrificial layer is developed. Fourthly, palladium is coated using sputtering. 3 nm–thick Cr layer is coated before palladium to ensure good adhesion between SU–8 and palladium. Finally, the sacrificial layer is removed. The fabrication flow is given in Fig. 4.5.

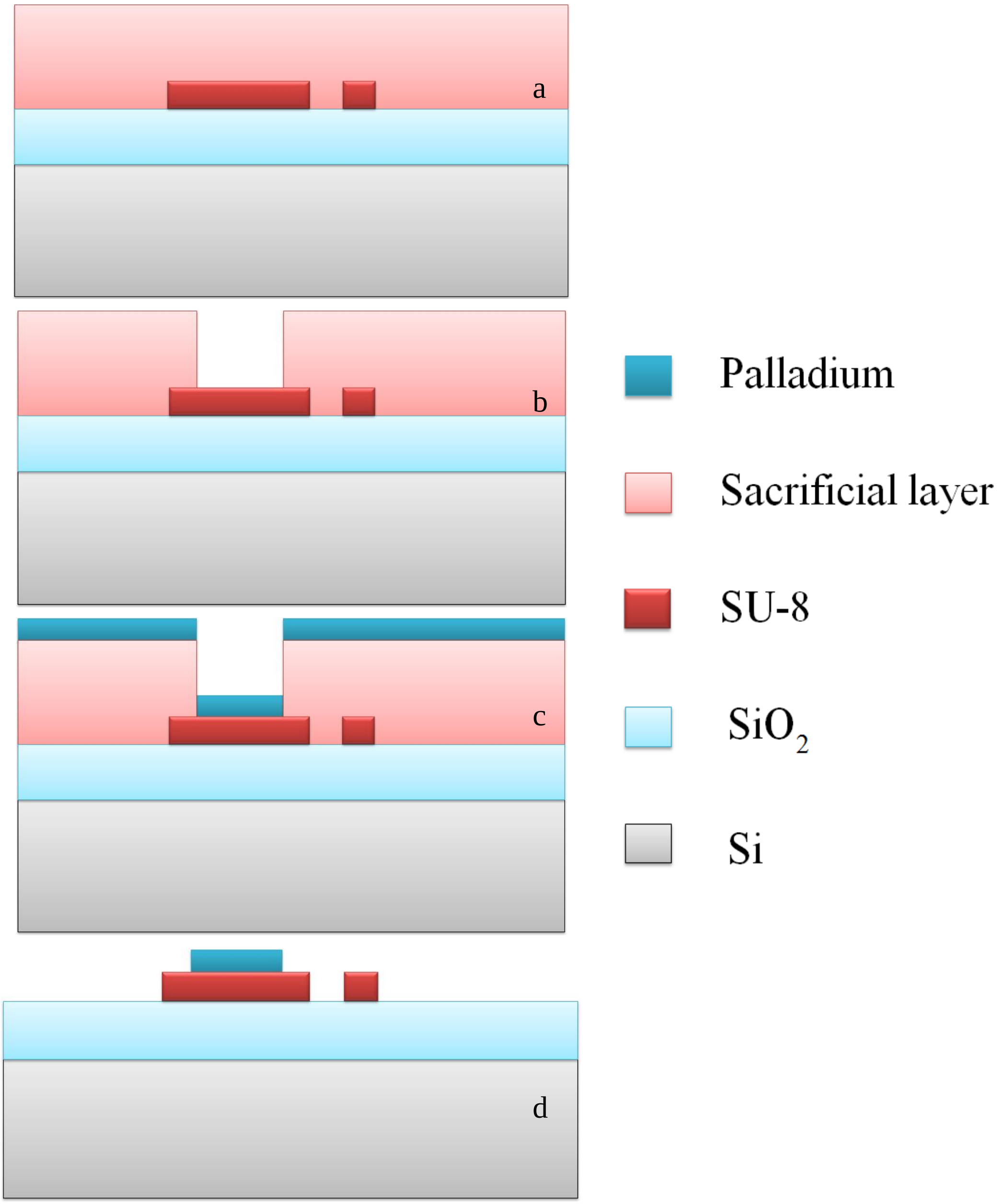

Figure 4.5 Lift–off steps of palladium coating. a) Spin-coating of sacrificial photoresist layer. b) Exposure and development of sacrificial photoresist. c) Palladium sputtering. d) Removal of sacrificial photoresist.

Fabricated palladium coating on the SU–8 layer is concentric with SU–8 microdisk so that there is no palladium at the edge of the SU–8 microdisk, where the optical mode propagates (see Fig. 4.6). This is important to have less absorption loss, therefore Q–factor of the SU–8 microdisk does not change. In addition, the lift–off was successful since the palladium layer has a good contrast.

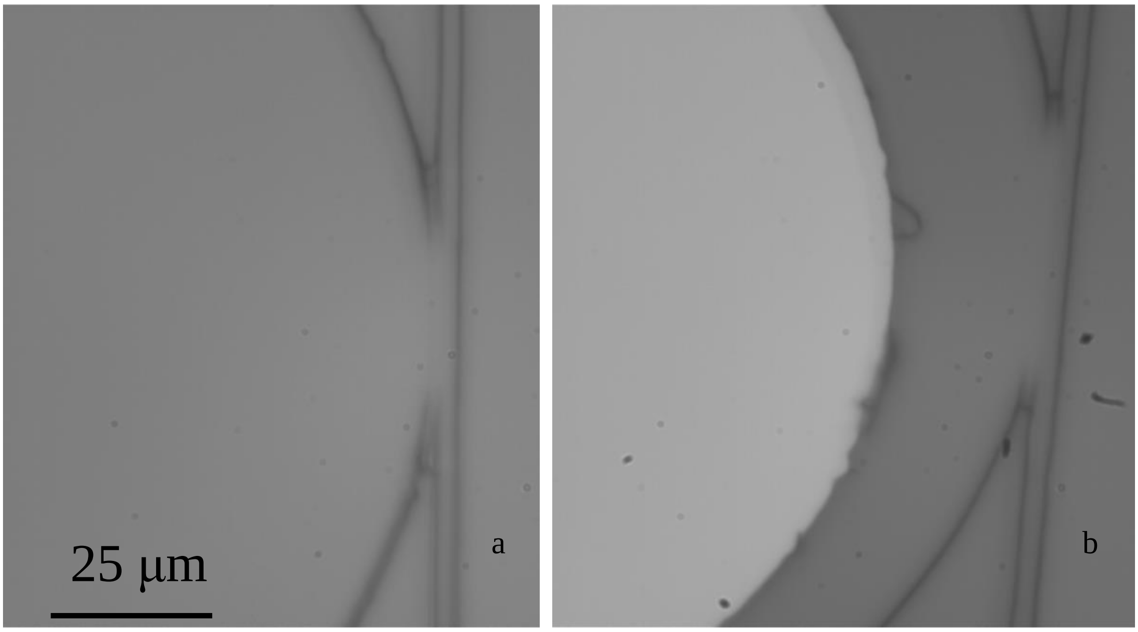

Figure 4.6 a) SU–8 microdisk and b) SU–8 microdisk with palladium coating.

4.4 Fabrication of Microdisk/Microring and Waveguide Structures Using Laser Writing Technique

The Q–factors of resonators fabricated using UV lithography are limited by the scattering loss due to the surface roughness of the resonators. Improving Q–factors is essential for having more sensitive devices. This can be achieved by fabricating the optical resonators using more sophisticated fabrication techniques such as two-photon polymerization (TPP). Although TPP is a slow method of fabrication, it is preferable to obtain resonators with much smoother surfaces. In this case, SU–8 layer absorbs two red photons at once with a nonlinear process requiring a relatively high light intensity. Therefore a red femtosecond laser is used for TPP (785 nm, 100 fs). The laser light is focused on the SU–8 layer and then the sample is moved precisely using a fine piezoelectric translation stage. Once the layer absorbs two photons with wavelength 785 nm, the effective wavelength becomes half of it, 392.5 nm. This effective wavelength is appropriate for cross–linking of SU–8, since it is sensitive to UV light.

TPP is a nonlinear process, which depends dramatically on the intensity. If the intensity is lower than a certain critical value, the SU–8 layer is not cross–linked, and it is cross–linked, if it remains in the focal volume (voxel) of the laser light. This gives a good contrast between the exposed and unexposed regions of SU–8, which ultimately results much smoother resonator surfaces.

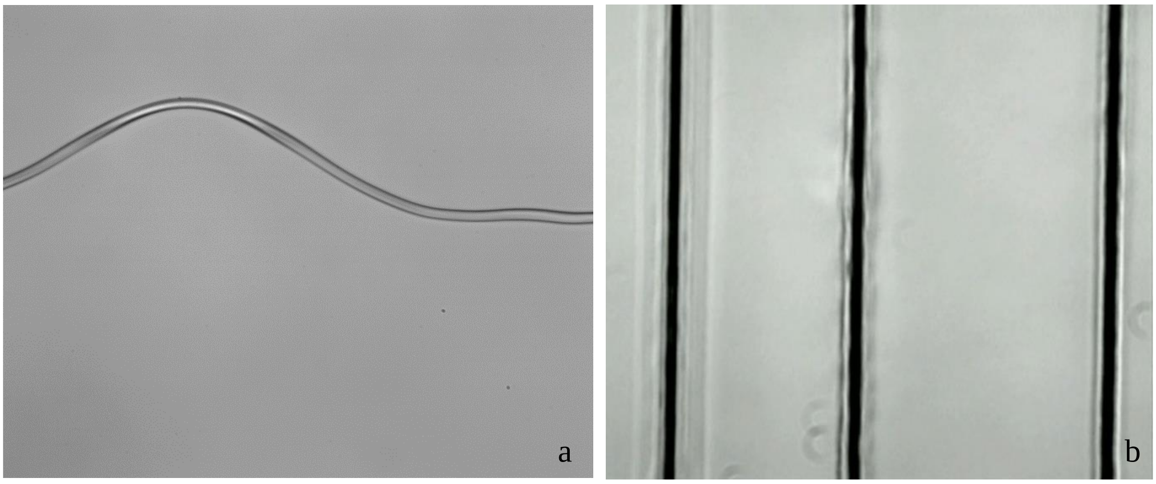

Figure 4.7 a) A waveguide fabricated using 80 mW power and 5 mm/s speed. Some parts of the waveguide come off because the exposure energy is insufficient. b) Burn marks produced with 120mW laser power. The speeds from left to right are 0.2, 0.5 and 1.0 mm/s.

The fabrication procedure is as follows: Glass substrates are cleaned using plasma cleaning for 10 minutes and coated with SU–8 2002 with 3000 rpm for 60 seconds to obtain 2 µm–thicknesses. Then a UV laser is used for the fabrication of waveguides. The laser light is focused on the SU–8 layer and swept with different power and speed values to find the optimum fabrication conditions (30–120 mW; 0.2–5.0 mm/s).

If the laser power is not sufficient or the speed is not low enough, the cross–linking of SU–8 and the adhesion of SU–8 to glass is not satisfactory. Therefore, in this case, the waveguides comes off from the glass (see Fig. 4.7-a). On the other hand, very high power or very slow speed causes burning in the SU–8 layer and cross–linking in a very wide area of SU–8 (see Fig. 4.7-b).

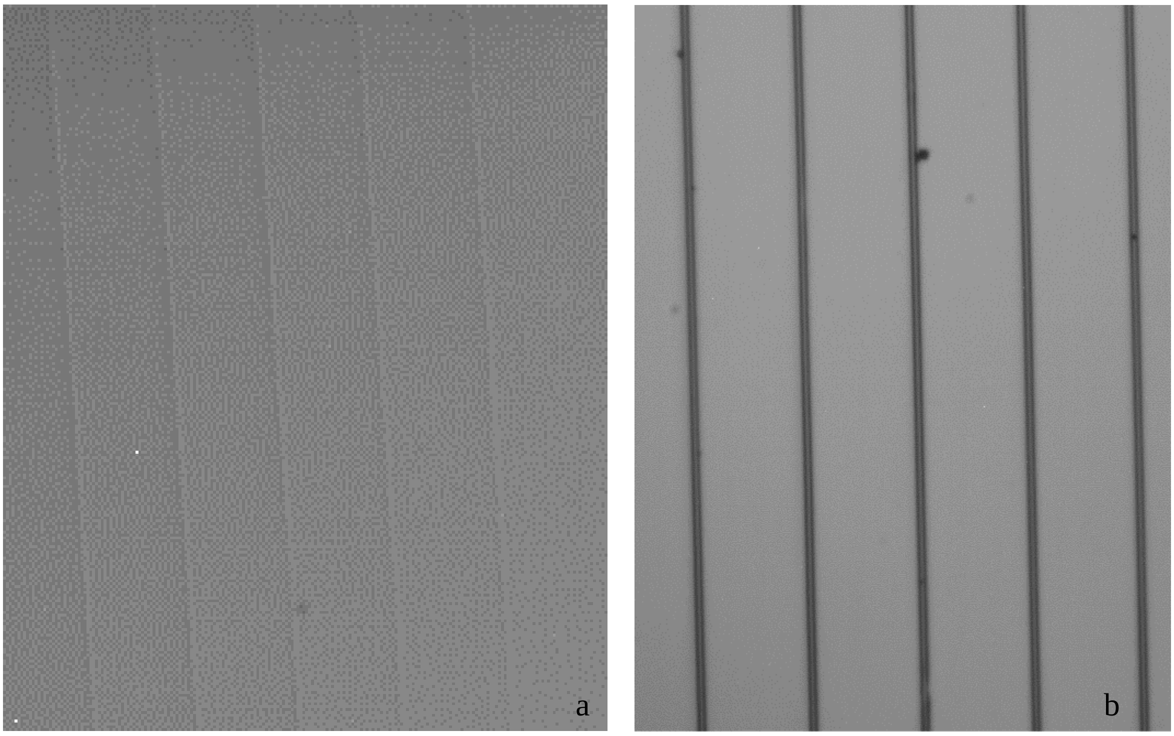

Figure 4.8 Optical microscope images of the waveguides a) Right after the PEB b) Right after the development. The widths of the waveguides are 4.7 µm.

The best result for waveguide fabrication is obtained with 30 mW and 0.5 mm/s and these parameters are used for the fabrication of the waveguide in the final device. For the same fabrication parameters, the adhesion quality of the waveguides changed from day to day. Therefore Omnicoat, an adhesion promoter for SU–8, is coated between the substrate and the SU–8 layer for increased stability. After exposure PEB is applied at 100^{O}C for 10 minutes. It is better, in terms of fabrication quality, to use the same layer of SU–8 both for the waveguides and the resonators. Therefore TPP must be performed before the development step. Although the waveguides are not developed, it is possible to observe them in the optical microscope since the PEB step induces a small refractive index change in the SU–8 layer (see Fig. 4.8). This observation is required to acquire precise control over the position of the resonator and the gap between the waveguide and the resonator.

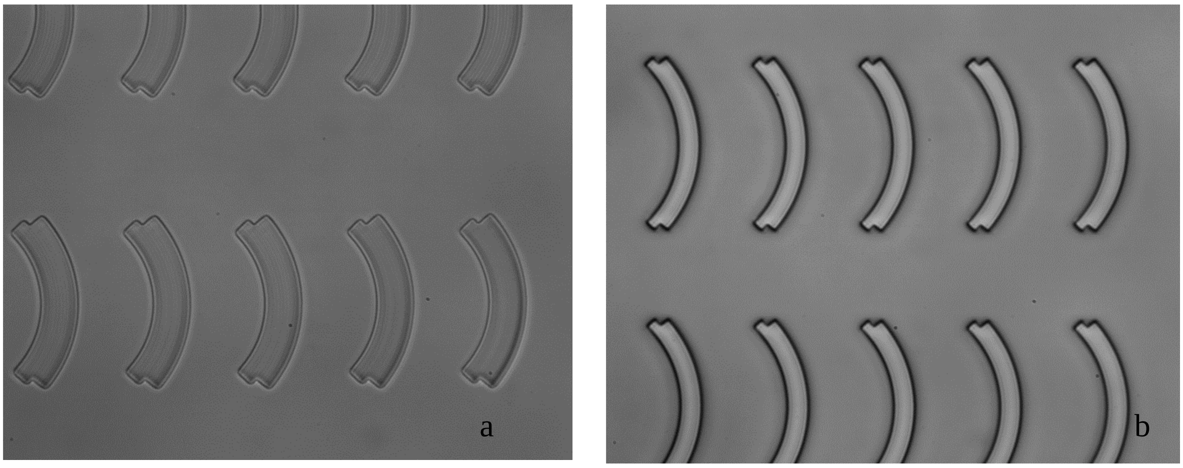

Figure 4.9 a) Fabricated arcs with speed 24 µm/s, linewidth 0.5 µm and power 7 mW. The individual writing lines are observable because these lines are too much separated from each other. b) Fabricated arcs with the same parameters in case a, except only the linewidth is changed to 0.3 µm. The surface is much smoother in this case.

Three different variables are changed to obtain the optimum fabrication parameters of resonators: The writing speed (6–24 µm/s), the linewidth (separation between two consecutive writing lines, 0.3 µm–0.7 µm) and laser power (3–7 mW). If the linewidth is not small enough, then the individual writing lines can be observed, which makes the resonator surface rough (see Fig. 4.9-a). The best result for resonator fabrication is obtained with a speed of 24 µm/s, a linewidth of 0.3 µm and a power of 7 mW (see Fig. 4.9-b).

Fabrication of waveguides and resonators introduces an extra width to the structure. In the waveguide case, the extra width is measured to be 2.35 µm; therefore the fabricated waveguide has a width of 4.7 µm. The extra width for the resonator is smaller, 0.25 µm. These extra thicknesses are important for the control over the gap between the waveguide and the resonator. For instance, if the gap is designed to be 1 µm, then the distance between them must be (2.35 + 0.25 + 1.00) µm = 3.60 µm. From the SEM image, we see that this design method results the right separation (see Fig. 4.10).

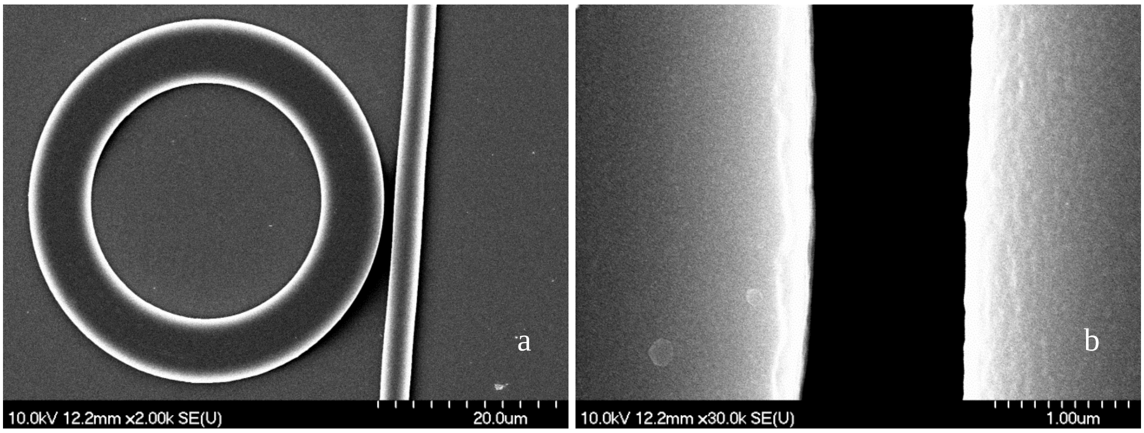

Figure 4.10 a) SEM image of a waveguide–resonator pair. b) Closer view of the gap region. The gap is designed to be 1 µm.

Chapter 5

EXPERIMENTAL SETUP AND RESULTS

Two experimental setups are used in the sensing experiments. The first setup is for achieving coupling to waveguides, preparing portable devices and measuring transmission spectra and the second setup is for testing the gas sensing capabilities of the portable devices in a gas chamber. In parallel, another setup is used for sensor device fabrication using laser writing technique.

5.1 Transmission Spectrum Measurement Setup

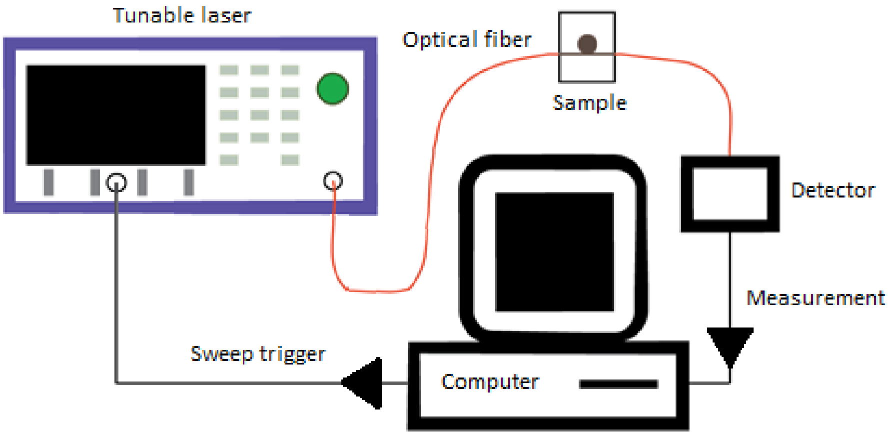

Figure 5.1 Sketch of the transmission spectrum measurement setup.

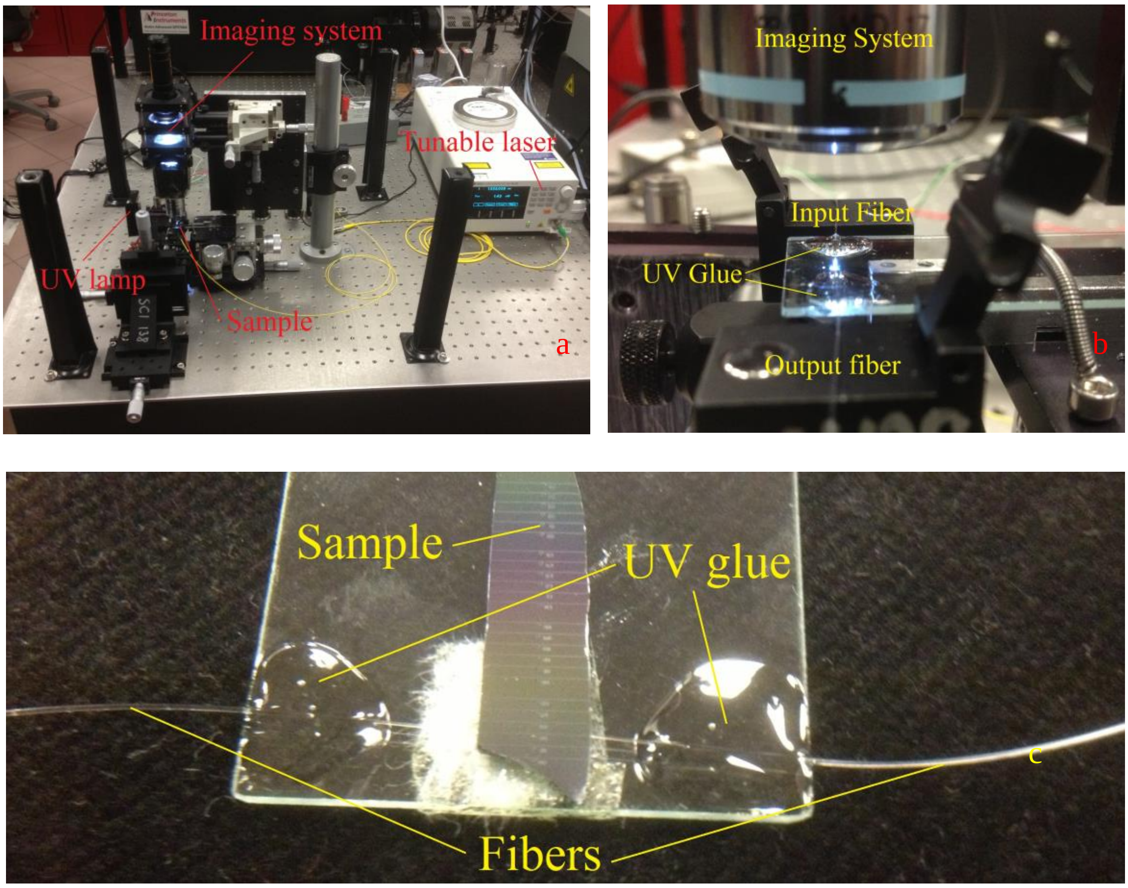

Figure 5.2 Transmission spectrum setup. a) General view of the setup. b) Closer view of fibers fixed with UV–curable glue. c) A portable device with coupled fixed fibers.

Laser light at telecom wavelength is produced using a tunable semiconductor laser and then coupled from an optical fiber to microfabricated SU–8 waveguides using end–face coupling. Once the coupling is achieved, the fibers are fixed to the sample with UV–curable glue so that portable devices are obtained. It is important to have portable devices for sensing experiments (see Fig. 5.2).

5.2 Experimental Results of Coupling to WGMs of SU–8 Microdisks

Two fabrication methods have been performed to obtain optical resonators. The first method is standard UV lithography and the second one is the two–photon polymerization (TPP) technique.

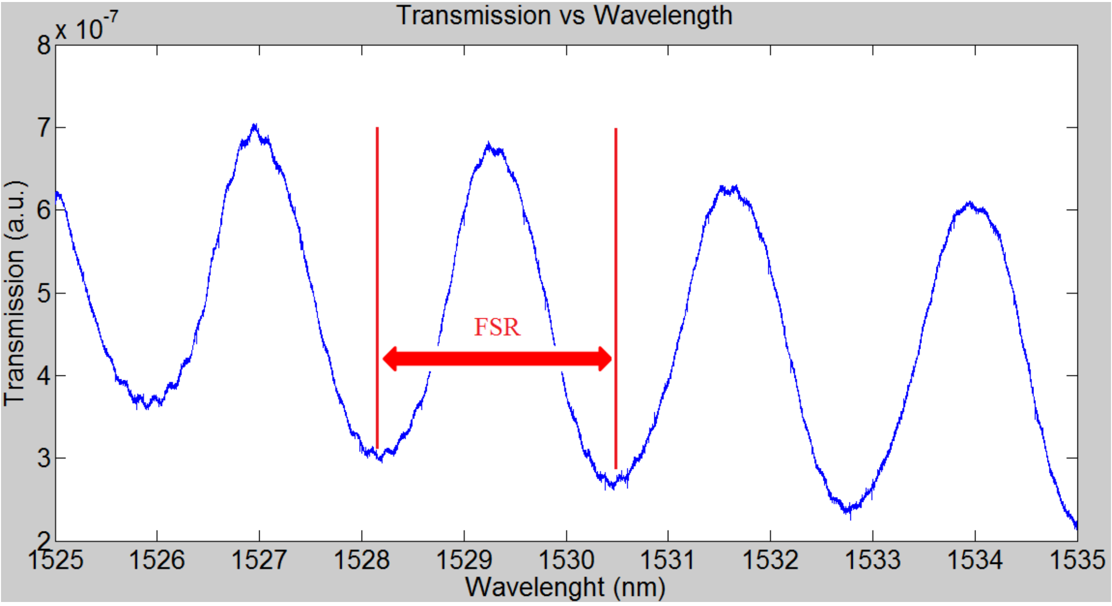

Figure 5.3 Transmission spectrum obtained from a 200 μm–diameter SU–8 optical microdisk.

5.2.1 Samples Fabricated Using UV Photolithography

Coupling to WGMs of SU–8 optical microdisk resonators are achieved in two steps. First, laser light is coupled from an optical fiber to SU–8 optical waveguide using end–face coupling method. Then the wavelength of the laser is swept in a certain interval so that we can observe resonance and out–of–resonance states consecutively. If the wavelength of the laser corresponds to a resonance wavelength, then there will be little transmission for this wavelength. On the other hand, if the wavelength of the laser is not a resonance wavelength, there will be no coupling to WGMs of microdisk and all of the light will be transmitted through the waveguide. The transmitted power is collected by another optical fiber and the coupling between the waveguide and the fiber is achieved using end–face coupling. A transmission spectrum of an SU–8 optical microdisk is given in Fig. 5.3.

The free spectral range (FSR) is measured to be 2.331 ± 0.059 nm, which is in agreement with the same configuration in the literature (2.28 ± 0.08 nm) [48]. Calculation of FSR is given in by the following formula:

$$FSR = \Delta\lambda = \frac{\lambda_0^2}{2\pi a n_{eff}} \tag{5.1}$$

where $\lambda_0 = 1530$ nm is the resonance wavelength in vacuum, $a = 100$ μm is the radius of the microdisk and $n_{eff} = 1.545$ is the effective refractive index for the fundamental mode in SU–8 [49], which gives $FSR = 2.411$ nm. The calculation is also in agreement with the measurement and the result from the literature [48].

Some small fluctuations are observed in the transmission spectrum. This can be attributed to the multimode operation of the waveguides, since the singlemode operation is not possible for waveguide dimensions higher than 1.5 μm by 1.5 μm [49].

The transmission spectrum is also measured for a palladium–coated SU–8 microdisk (See Fig. 5.4). The FSR and the positions of the resonance wavelengths are not changed, which means that the palladium coating does not interfere with the WGM propagating at the edge of the microdisk.

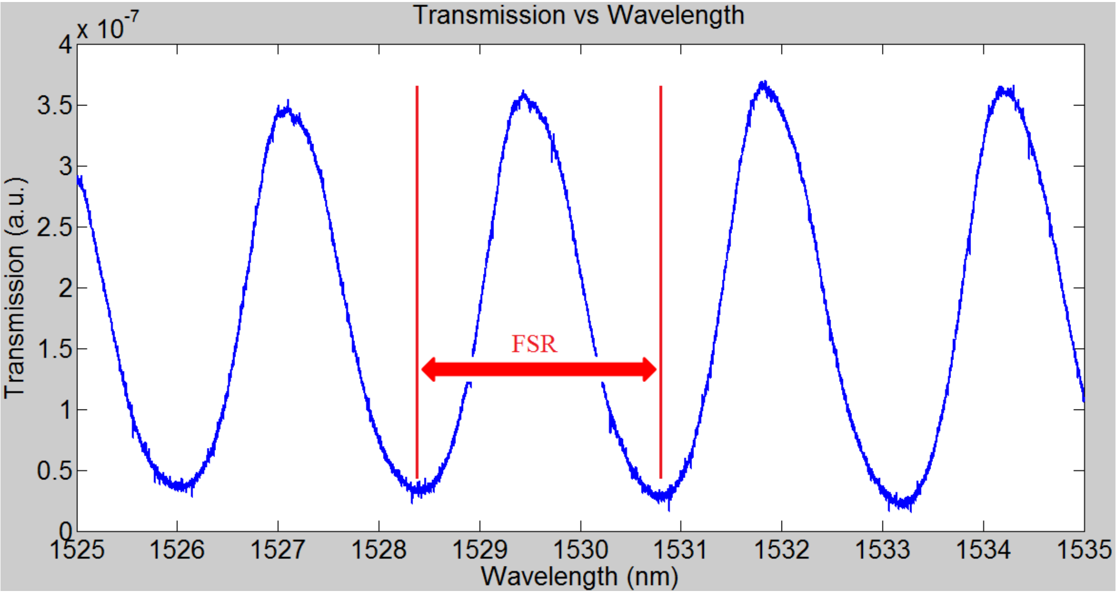

Figure 5.4 Transmission spectrum measured from a palladium–coated SU–8 microdisk.

5.2.2 Samples Fabricated Using TPP

The optical characterization of TPP–fabricated waveguide-resonator pairs is performed by coupling tunable infrared laser light to the waveguide and measuring the transmission spectrum (see Fig. 5.5). The Q–factor is measured to be 100-120 and the free spectral range (FSR) to be 27.465 ± 1.078 nm. Relatively small Q–factor values are attributed to the small size of the resonators, which is dictated by the writing range of the piezoelectric translation stage and relatively small refractive index contrast between SU–8 and glass. FSR is calculated with the same method used in calculating FSR of UV photolithography samples. Since the wavelength region is wider in this case, two FSR values are calculated. One for λ=1500 nm and one for λ=1590 nm and FSR values are found to be 15.452 and 17.362 nm respectively. Since these values are smaller than the measured FSR values, this might be due to a smaller n_{eff}.

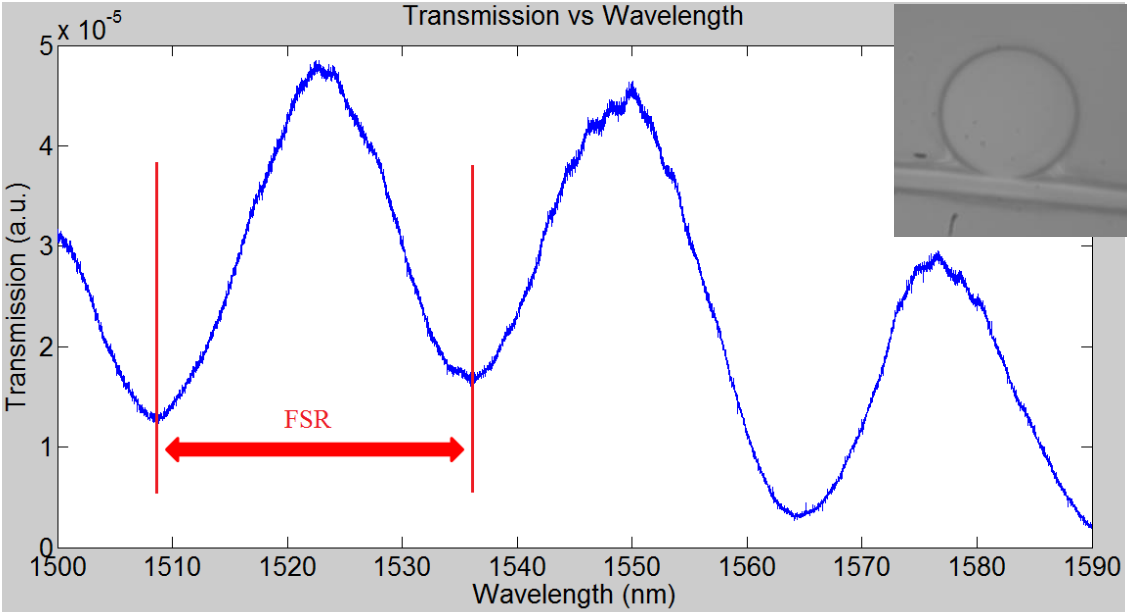

Figure 5.5 Transmission spectrum obtained from a TPP–fabricated sample. The optical microscope image of the sample is given in the inset. The radius of the microdisk is designed to be 15 μm.

Two solutions can be considered to increase the small Q–factors of TPP samples:

1. Fabricating bigger resonators: Small resonators are fabricated because the writing process was time–consuming and the travelling range of the piezoelectric translation stage was limited. However, bigger microdisks can be fabricated by sacrificing from the fabrication time. This will allow obtaining a larger bending radius therefore higher Q–factors.

2. Fabricating mushroom–shaped geometries: Since the refractive indices of glass and SU–8 are very close, separating the SU–8 layer from the glass surface will increase the Q–factors while keeping the size unchanged (See Fig. 5.6). Mushroom–shaped structure can be defined using TPP since it allows structures written in all three dimensions.

Although defining more layers in the transverse direction will consume some more time, the microdisk will have higher–Q which ultimately increases the sensitivity of the device.

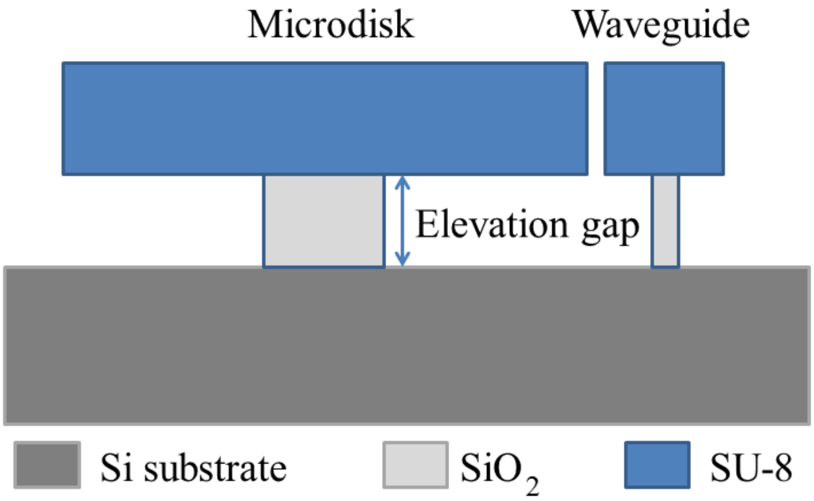

Figure 5.6 Designed mushroom–shaped geometry for separating the microdisk resonator from the substrate to introduce higher refractive index contrast.

5.3 Gas Sensing Setup

Gas sensing setup is built for testing the hydrogen gas detection ability of the portable devices (see Fig. 5.7). 1% hydrogen–99% nitrogen gas mixture and pure nitrogen are sent to the gas flow controllers and then mixed to obtain 100 ppm to 1% hydrogen concentration in the gas chamber. The gas chamber is designed to have gas inlets and outlets as well as the fiber inlets and outlets for the input and output laser light. The gas sensing experiments are still in progress and the resonance wavelength shifts will be measured.

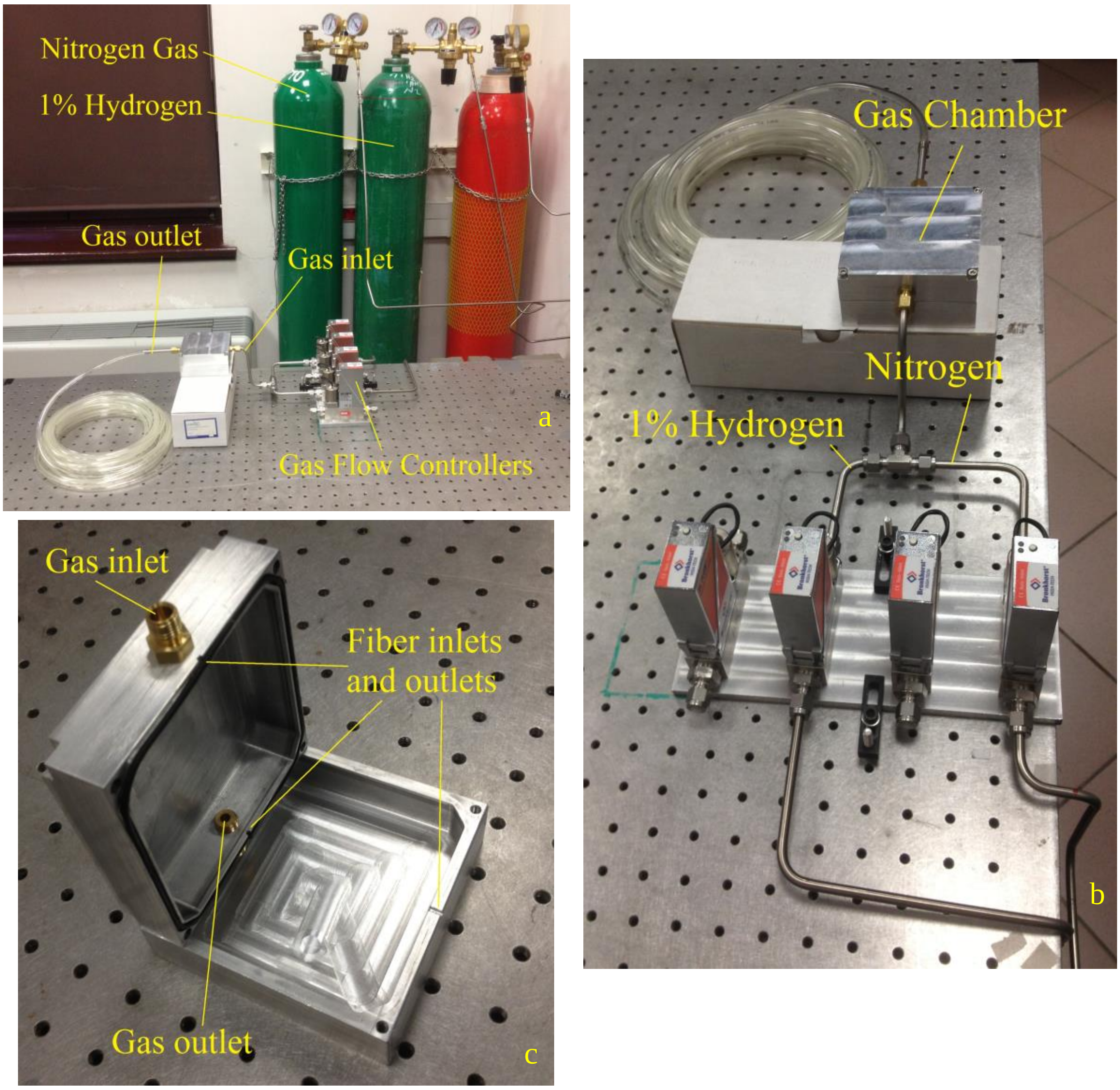

Figure 5.7 Gas sensing experiment setup. a) General view of the setup. b) Closer view of gas flow controllers. c) Closer view of the gas chamber.

5.4 Laser Writing Setup

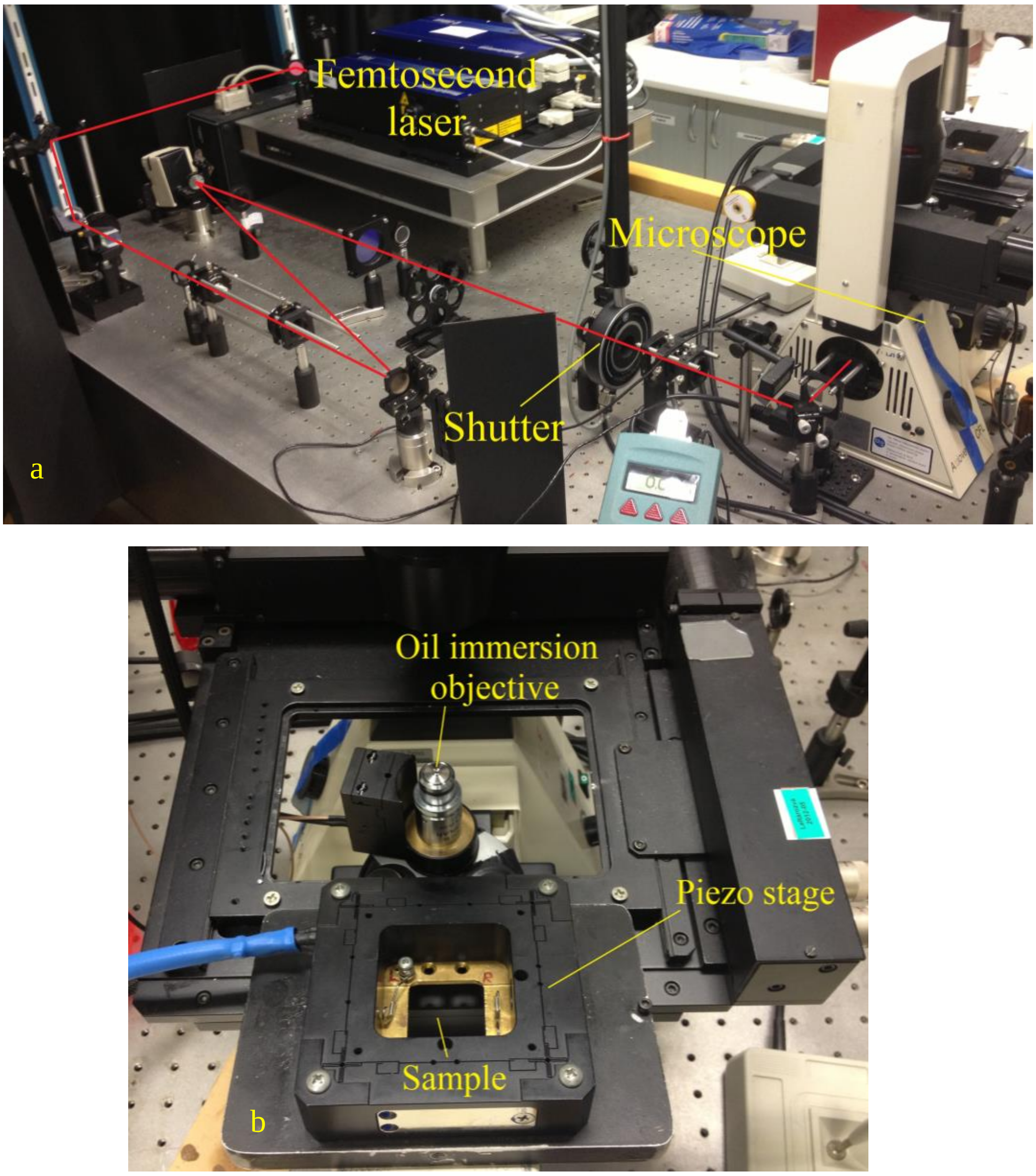

Figure 5.8 a) General view of the TPP setup. The path of the laser light is denoted by red lines. b) Closer view of the sample area.

The TPP experiments are performed using a femtosecond fiber laser with wavelength 785 nm. The laser light is sent through a shutter and to an oil immersion microscope objective (see Fig. 5.8-a). Then a piezoelectric translation stage is placed on the objective with the sample. After the laser light is focused on the sample, the piezoelectric translation stage is moved using computer control to write the desired structures (see Fig. 5.8-b). The shutter is closed and opened at the necessary steps to avoid overexposure on the SU–8 layer.

Chapter 6

CONCLUSIONS AND OUTLOOK

A hydrogen gas detection method using SU–8 polymer optical microdisk resonators is presented. The fabrication procedures, theory of WGMs, experimental setups and results are discussed together with a review of hydrogen gas sensing technologies in the literature. Transmission measurements are obtained from microdisk resonators fabricated using UV photolithography and TPP. UV photolithography samples are measured both with and without palladium coating. The resulting maximum Q–factor is 2000, being mainly limited by the scattering loss induced by the surface roughness of the samples. TPP method is also considered to fabricate the resonators. The maximum observed Q–factor from TPP samples is 120, which is lower than the UV photolithography samples. These low Q–factors are attributed to small bending radii of the resonators and small refractive index contrast between the substrate and SU–8. Although this value is small, the optical microscope and SEM images show promising results, since the surfaces of the resonators are very smooth. When fabricated, higher–Q resonators can be employed for sensing very low hydrogen concentrations (down to 100 ppm).

After light coupling is achieved to UV photolithography samples, the input and output fibers are fixed therefore portable devices are obtained. In the future, these portable devices will be tested in the gas chamber for hydrogen gas detection by measuring the resonance shifts upon hydrogen gas exposure. COMSOL simulations will be performed to observe how the effect of expansion of palladium will be transferred to the expansion of SU–8 microdisks and the relation between the resonance shifts and the hydrogen concentration will be derived. Higher Q–factors will be pursued by fabricating mushroom–shaped geometries using two–photon polymerization setup. Grating coupler method will be employed for coupling the light to waveguide, since it has higher alignment tolerance. Add-drop filter design can be employed to have higher signal-to-noise ratio. Finally, other explosive gases like methane, ethane and propane will be tested for detection.

APPENDIX A

MATLAB CODE FOR FIG. 3.4

Resonance wavelengths for different radii of the microdisk resonators

```
% Main code

lambda = 0.36:0.01:12.8;
n0 = arrayfun (@(x) findn(x), lambda);
k0 = 2*pi./lambda;

xmq=[15.635,16.667,17.778,18.810,20.000,21.032,22.222,23.333,24.444,25.39
7,...
26.508,27.540,28.651,29.683,30.794,31.905,32.937,33.810,35.000,36.032,...
37.222,38.175,39.206,40.317,41.349,42.460,43.492,44.603,45.635,46.731,...
47.692,48.846,49.762,50.762,51.905,53.048,54,55.048,56.1,57.238,58.037,..
.
59.167,60.256,61.282,62.308,63.333,64.423,65.513,66.538,67.564];

kzvalues = arrayfun (@(x) findkz(x), lambda);

xmqvslambda = zeros ( (length (xmq) + 1) , (length (lambda) + 1));
xmqvslambda( (length (xmq) + 1) , : ) = [lambda 0];
R = zeros(size(k0));

for ii = 1:length(xmq)

    R = xmq(ii)./(sqrt(k0.^2.*n0.^2-kzvalues.^2));
    plot (1000*lambda, 2000*R)
    hold on

    xmqvslambda(ii,:) = [R xmq(ii)];

end

axis ([900 1000 2000 5000])
xlabel('Wavelength (nm)');
```

```
ylabel('Diameter (nm)');


% Supplementary function “findkz”

function [smallestkz] = findkz (lambda)

d = 0.25;
n0 = findn (lambda);
k0 = 2*pi/lambda;

fun = @(kz) (sqrt(k0^2*(n0^2-1)-kz^2) - kz*tan(kz*d/2));

solarr = [];
ii = 1;
while length (solarr) < 1

    solarr = fzero (fun, ii);
    if solarr (1) < 0

        solarr = [];

    elseif isnan(solarr) == 1

        solarr = [];

    end
    ii = ii + 0.1;

end

smallestkz = solarr;


% Supplementary function “findn”

function n0 = findn (lambda)
lambda2=lambda*1000;
e = 1.2398/lambda2;
e0 = 3.65;
ed = 36.1;
eg = 1.424;
g = ed / (4*e0^3 * (e0^2 - eg^2));
ef = sqrt(2*e0^2 - eg^2);
y2 =1+g*(ef^4-eg^4)+2*g*(ef^2-eg^2)*e^2+2*g*e^4*log((ef^2 -e^2)/(eg^2-
e^2));
n0=sqrt(y2);
```

APPENDIX B

MEEP CODE FOR FIG. 3.1

MEEP simulation of the first three radial modes for a 20 µm–radius disk

```
(define-param w 1.541);wavelength
(define-param n 1.5);index of the material
(define-param df 0.001);distance between max and min frequency
(define-param nfreq 1000) ; number of frequencies at which to compute
flux
(define-param r 20.000) ; radius of microdisk
(define-param dpml 1) ; width of pml
(define-param wg 1) ; width of waveguide
(define-param d 0.510) ; distance
(define-param rs 10) ; resolution

(set! geometry-lattice (make lattice (size  (* 2 (+  r dpml wg d)) (* 2
(+ r dpml wg d)) no-size )))

(set! geometry (list

      (make cylinder
      (center 0 0 0)(radius r)(axis 0 0 1)(height infinity)
      (material (make dielectric(index n))))

      (make block
      (center 0  (* -1 (+ r d (/ wg 2))) 0)(size infinity wg infinity )
      (material (make dielectric(index n))))))


(set! sources (list
      (make source
            (src (make gaussian-src (wavelength w)(fwidth df)))
            (component Hz)
            (center (* -1 (+ r d (/ wg 2)))  (* -1 (+ r d (/ wg 2))) 0)
(size 0 wg 0))))

(set! pml-layers (list (make pml (thickness dpml))))
(set-param! resolution rs)

(define ref ; reference flux
      (add-flux (/ 1 w) df nfreq
```

```
                    (make flux-region
                      (direction X)
                      (center (+ (* -1 r) 0.5) (* -1 (+ r d (/ wg 2))) 0)
(size 0 (* 2 wg) 0))))


(define trans1 ; transmitted flux
      (add-flux (/ 1 w) df nfreq
                    (make flux-region
                      (direction X)
                      (center (* 1 r) (* -1 (+ r d (/ wg 2)))  0) (size 0
(* 2 wg) 0))))

(define trans2 ; flux in the disk
      (add-flux (/ 1 w) df nfreq
                    (make flux-region
                      (direction Y)
                      (center (* -1 r) 0 0) (size (* 2 wg) 0 0))))



(run-sources+
      (stop-when-fields-decayed 50 Hz
            (vector3 (+ (* +1 r) 1) (* -1 (+ r d (/ wg 2))) 0) 1e-3)
      (at-beginning output-epsilon)
      (at-end  output-hfield-z)
      (at-every 60 (output-png Hz "-Zc bluered")))



(display-fluxes ref trans1 trans2)
```

Bibliography

1. Dincer, I., *Technical, environmental and exergetic aspects of hydrogen energy systems.* International Journal of Hydrogen Energy, 2002. **27**: p. 265-285.
2. Wang, M. and Feng, Y., *Palladium–silver thin film for hydrogen sensing.* Sensors and Actuators B: Chemical, 2007. **123**(1): p. 101-106.
3. Gupta, R.B., ed. *Hydrogen Fuel: Production, Transport and Storage*. 2009, CRC Press: Boca Raton.
4. Midilli, A., Ay, M., Dincer, I and Rosen, M.A., *On hydrogen and hydrogen energy strategies.* Renewable and Sustainable Energy Reviews, 2005. **9**(3): p. 255-271.
5. Hübert, T., Boon-Brett, L., Black, G and Banach, U., *Hydrogen sensors – A review.* Sensors and Actuators B: Chemical, 2011. **157**(2): p. 329-352.
6. Bévenot, X., Trouillet, A., Veillas, C., Gagnaire, H and Clément M., *Hydrogen Leak Detection Using an Optical Fibre Sensor for Aerospace Applications.* Sensors and Actuators B: Chemical, 2000. **67**: p. 57-67.
7. Aroutiounian, V., *Metal oxide hydrogen, oxygen, and carbon monoxide sensors for hydrogen setups and cells.* International Journal of Hydrogen Energy, 2007. **32**(9): p. 1145-1158.
8. Song, J and Lu, W., *Operation of Pt/AlGaN/GaN Heterojunction Field-Effect-Transistor Hydrogen Sensors With Low Detection Limit and High Sensitivity.* IEEE Electron Device Letters, 2008. **29**: p. 1193-1195.
9. Boon-Brett, L., Black, G., Moretto, P and Bousek, J., *A comparison of test methods for the measurement of hydrogen sensor response and recovery times.* International Journal of Hydrogen Energy, 2010. **35**(14): p. 7652-7663.
10. Jessop, G., *Katharometers.* Journal of Scientific Instruments, 1966. **43**: p. 777-782.

11. Lee, E.-B., Hwang, I.-S., Cha, J.-H., Lee, H.-J., Lee, W.-B., Pak, J.J., Lee, J.-H. and Ju, B.-K., *Micromachined catalytic combustible hydrogen gas sensor.* Sensors and Actuators B: Chemical, 2011. **153**(2): p. 392-397.

12. Matsumiya, M., Qiu, F., Shin, W., Izu, N., Murayama, N. and Kanzaki, S., *Thin Film Li Doped NiO for Thermoelectric Hydrogen Gas Sensor.* Thin Solid Films, 2002. **419**: p. 213-217.

13. Qiu, F., Shin, W., Matsumiya, M., Izu, N., Matsubara, I and Murayama, N., *Miniaturization of thermoelectric hydrogen sensor prepared on glass substrate with low-temperature crystallized SiGe film.* Sensors and Actuators B: Chemical, 2004. **103**(1-2): p. 252-259.

14. Hu, H., Luan, W., Zhang, J.-S., Qi, Y.-S. and Tu, S.-T., *Thermoelectric hydrogen sensor working at room temperature prepared by bismuth–telluride P–N couples and Pt/γ-Al2O3.* Sensors and Actuators B: Chemical, 2008. **128**(2): p. 581-585.

15. Favier, F., Walter, E.C., Zach, M.P., Benter, T. and Penner, R.M., *Hydrogen sensors and switches from electrodeposited palladium mesowire arrays.* Science, 2001. **293**(5538): p. 2227-31.

16. Yu, X., Li, C., Low, Z.N., Lin, J., Anderson, T.J., Wang, H.T., Ren, F., Wang, Y.L., Chang, C.Y., Pearton, S.J., Hsu, C.H., Osinsky, A., Dabiran, A., Chow, P., Balaban, C. and Painter, J., *Wireless hydrogen sensor network using AlGaN/GaN high electron mobility transistor differential diode sensors.* Sensors and Actuators B: Chemical, 2008. **135**(1): p. 188-194.

17. Dong, S., Bai, F., Li, J. and Viehland, D., *Sound Resonance Hydrogen Sensor.* Applied Pyhsics Letters, 2003. **82**: p. 4590-4592.

18. Lomperski, S., Anselmi, M. and Huhtiniemi, I., *Ultrasonic and Resistive Hydrogen Sensors for Inert Gas Water Vapour Atmospheres.* Measurement Science and Technology, 2000. **11**: p. 518-525.

19. Madou, M.J., ed. *Fundamentals of Microfabrication: The Science of Miniaturization*. 2 ed. 2002, CRC Press: Boca Raton, London, New York, Washington.
20. Chou, Y.-I., Chiang, H.-C. and Wang, C.-C., *Study on Pd functionalization of microcantilever for hydrogen detection promotion.* Sensors and Actuators B: Chemical, 2008. **129**(1): p. 72-78.
21. Baselt, D.R., Fruhberger, B., Klaassen, E., Cemalovic, S., Britton Jr, C.L., Patel, S.V., Mlsna, S.V., McCorkle, D and Warmack, B., *Design and Performance of a Microcantilever Based Hydrogen Sensor.* Sensors and Actuators B: Chemical, 2003. **88**: p. 120-133.
22. Butler, M.A., *Optical Fiber Hydrogen Sensor.* Applied Physics Letters, 1984. **45**(10): p. 1007-1009.
23. Maciak, E. and Opilski, Z., *Transition metal oxides covered Pd film for optical* H_2 *gas detection.* Thin Solid Films, 2007. **515**(23): p. 8351-8355.
24. Farahi, F., Leilabady, P.A., Jones, J.D.C. and Jackson, D.A., *Interferometric Fibre Optic Hydrogen Sensor.* Journal of Physics E: Scientific Instruments, 1987. **20**: p. 432-434.
25. Homola, J., ed. *Surface Plasmon Resonance Based Sensors*. 2006, Springer: Berlin, Heidelberg, New York.
26. Bévenot, X., Trouillet, A., Veillas, C., Gagnaire, H. and Clément, M., *Surface Plasmon Resonance Hydrogen Sensor Using An Optical Fibre.* Measurement Science and Technology, 2002. **13**: p. 118-124.
27. Tittl, A., Mai, P., Taubert, R., Dregely, D., Liu, N and Giessen, H., *Palladium-based plasmonic perfect absorber in the visible wavelength range and its application to hydrogen sensing.* Nano Letters, 2011. **11**(10): p. 4366-9.

28. Lin, K., Lu, Y., Chen, J., Zheng, R., Wang, P. and Ming, H., *Surface Plasmon Resonance Hydrogen Sensor Based on Metallic Grating with High Sensitivity.* Optics Express, 2008. **16**(23).
29. Elisabetta Comini, G.F., Giorgio Sberveglieri, ed. *Solid State Gas Sensing*. 2009, Springer: New York.
30. Fukai, Y., ed. *The Metal-Hydrogen System: Basic Bulk Properties*. 1993, Springer: Heidelberg.
31. Kılınç, N., *Resistive Hydrogen Sensors Based on Nanostructured Metals and Metal Alloys.* Nanoscience and Nanotechnology Letters, 2013. **5**(8): p. 825-841.
32. Burch, R. and Lewis, F.A., *The Form of the Interaction Between Palladium and Hydrogen.* Platinum Metals Review, 1971. **15**(1): p. 21-25.
33. Noh, J.-S., Lee, J.M. and Lee, W., *Low-dimensional palladium nanostructures for fast and reliable hydrogen gas detection.* Sensors (Basel), 2011. **11**(1): p. 825-51.
34. Rayleigh, L., *The Problem of the Whispering Gallery.* Philosophical Magazine, 1910. **20**: p. 1001-1004.
35. Sennaroğlu, A., ed. *Photonics and Laser Engineering: Principles, Devices and Applications*. 2010, McGraw Hill: New York.
36. *Meep*. 2012; Available from: http://ab-initio.mit.edu/wiki/index.php/Meep.
37. Kiraz, A., *Nonclassical Light Emission from Single Self-Assembled InAs Quantum Dots*, 2002, University of California Santa Barbara, USA.
38. Pan, Y.-L. and Chang, R.K., *Highly efficient prism coupling to whispering gallery modes of a square μ cavity.* Applied Physics Letters, 2003. **82**(4): p. 487.
39. Jonáš, A., Karadag, Y., Mestre, M. and Kiraz, A., *Probing of Ultrahigh Optical Q-factors of Individual Liquid Microdroplets on Superhydrophobic Surfaces Using Tapered Optical Fiber Waveguides.* Journal of Optical Society of America B, 2012. **29**: p. 3240-3247.

40. Yariv, A., *Universal relations for coupling of optical power between microresonators and dielectric waveguides.* Electronics Letters, 2000. **36**(4): p. 321.
41. Ang, T.W., Reed, G.T., Vonsovici A., Evans, A.G.R., Routley, P.R. and Josey, M.R., *Effects of Grating Heights on Highly Efficient Unibond SOI Waveguide Grating Couplers.* IEEE Photonics Tecnology Letters, 2000. **12**(1): p. 59-61.
42. Taillaert, D., Van Laere, F., Ayre, M., Bogaerts, W., Van Thourhout, D., Bientsman, P. and Baerts, R., *Grating Couplers for Coupling between Optical Fibers and Nanophotonic Waveguides.* Japanese Journal of Applied Physics, 2006. **45**(8A): p. 6071-6077.
43. Liu, J., Cai, B., Zhu, J., Ding, G., Zhao, X., Yang, C. and Chen, D., *Process research of high aspect ratio microstructure using SU-8 resist.* Microsystem Technologies, 2004. **10**(4): p. 265-268.
44. Altpeter, D.M., *Description of SU-8.* University of Twente, Netherlands, 2005.
45. Dai, D., Yang, L., Sheng, Z., Yang, B. and He, S., *Compact Microring Resonator with 2x2 Tapered MMI Couplers.* Journal of Lightwave Technology, 2009. **27**(21): p. 4878-4883.
46. Vahala, K., ed. *Optical Microcavities*. 2004, World Scientific: Singapore.
47. *SU-8 2000 Permanent Epoxy Negative Photoresist Processing Guidelines.* Microchem, Newton, MA, USA
48. Cho, S.-Y. and Jokerst, N.M., *A Polymer Microdisk Photonic Sensor Integrated onto Silicon.* IEEE Photonics Tecnology Letters, 2006. **18**: p. 2096-2098.
49. Hammer, M. *1-D Multilayer Slab Waveguide Mode Solver*. 2013; Available from: http://www.computational-photonics.eu/oms.html.

Vita

Mustafa ERYÜREK received his B. Sc. degree from Department of Physics, Bilkent University, Ankara, Turkey. He later joined the M. Sc. in Optoelectronics and Photonics Engineering program at Koç University, Istanbul, Turkey. For his M. Sc. degree thesis he worked on “Hydrogen Gas Sensor Based on a Polymer Optical Microdisk Resonator”. He orally presented this work in a national conference, NANO-TR 2013. He expects to pursue his Ph. D. degree at Koç University, Department of Physics.